



**ORTHOGONAL FREQUENCY DIVISION
MULTIPLEXED WAVEFORM
EFFECTS ON PASSIVE BISTATIC RADAR**

THESIS

Forrest D. Taylor, Maj, USAF

AFIT-ENG-MS-19-M-058

**DEPARTMENT OF THE AIR FORCE
AIR UNIVERSITY**

AIR FORCE INSTITUTE OF TECHNOLOGY

Wright-Patterson Air Force Base, Ohio

DISTRIBUTION STATEMENT A
APPROVED FOR PUBLIC RELEASE; DISTRIBUTION UNLIMITED.

The views expressed in this document are those of the author and do not reflect the official policy or position of the United States Air Force, the United States Department of Defense or the United States Government. This material is declared a work of the U.S. Government and is not subject to copyright protection in the United States.

AFIT-ENG-MS-19-M-058

ORTHOGONAL FREQUENCY DIVISION MULTIPLEXED WAVEFORM
EFFECTS ON PASSIVE BISTATIC RADAR

THESIS

Presented to the Faculty
Department of Electrical and Computer Engineering
Graduate School of Engineering and Management
Air Force Institute of Technology
Air University
Air Education and Training Command
in Partial Fulfillment of the Requirements for the
Degree of Master of Science in Electrical Engineering

Forrest D. Taylor, B.S.E.E., M.S.A.E.

Maj, USAF

March 2019

DISTRIBUTION STATEMENT A
APPROVED FOR PUBLIC RELEASE; DISTRIBUTION UNLIMITED.

AFIT-ENG-MS-19-M-058

ORTHOGONAL FREQUENCY DIVISION MULTIPLEXED WAVEFORM
EFFECTS ON PASSIVE BISTATIC RADAR

THESIS

Forrest D. Taylor, B.S.E.E., M.S.A.E.
Maj, USAF

Committee Membership:

Maj James R. Lievsay, PhD
Chair

Dr. Julie A. Jackson
Member

Dr. Michael A. Temple
Member

Abstract

Communication waveforms act as signals of opportunity for passive radars. However, these signals of opportunity suffer from range-Doppler processing losses due to their high range sidelobes and pulse-diverse waveform aspects. Signals such as the long term evolution (LTE) encode information within the phase and amplitude of the waveform. This research explores aspects of the LTE, such as the encoding scheme and bandwidth modes on passive bistatic Doppler radar. Signal space-time adaptive processing (STAP) performance is evaluated and parameters are compared with the signal to interference-plus-noise ratio (SINR) metric.

*Each moment find within yourself a greater understanding of the universe; a vision
to inspire you to continue to live and learn.*

Acknowledgements

I owe the greatest thanks to my loving wife. This research would not have been possible without her dedication to family and loving support. I would also like to thank my children for bravely facing the new challenges of each day, and for their wonderful smiles and playfulness that brightens our lives.

I also wish to thank the Air Force Institute of Technology (AFIT) radar faculty. I am grateful for the time and energy invested by most especially Maj James R. Lievsay, and Dr. Julie Jackson. From the beginning, Maj Lievsay carefully and meticulously guided me through the science of radar and its underpinning math. Dr Jackson and Maj Lievsay are doing amazing work to keep radar research active for the United States Air Force (USAF).

Throughout my time at AFIT, I was humbled by the mountain of knowledge we must climb in order to ask ourselves research questions. I am greatly privileged to have been selected for the radar education and research program, and I hope that my work is a worthwhile investment.

Forrest D. Taylor

Table of Contents

	Page
Abstract	iv
Acknowledgements	vi
List of Figures	ix
List of Tables	xi
List of Abbreviations	xii
I. Introduction	1
1.1 Problem Description	1
1.2 Research Motivation	1
1.3 Research Goal	2
1.4 Previous Works	2
II. Theory	5
2.1 Overview	5
2.2 OFDM and Communication Waveforms	5
2.2.1 The LTE OFDM	6
2.3 Radar: Fast and Slow-Time	11
2.3.1 Fast-Time	12
2.3.2 Slow-Time	15
2.4 Space-time Adaptive Processing	17
2.5 Clutter Ridge	24
2.6 Passive Bistatic Radar	25
III. Methodology	28
3.1 Overview	28
3.2 Generating the OFDM	28
3.3 Radar Model Assumptions	32
3.3.1 Symbol Extraction	33
3.3.2 Radar Bandwidth and Sample Rate Interpolation	34
3.4 STAP Assumptions	35
3.4.1 Geometry	36
3.4.2 Clutter	36
3.4.3 Filter Width	38

	Page
IV. Results & Analysis	40
4.1 Overview	40
4.2 Temporal Analysis	40
4.3 Random Bandwidth	45
4.4 Bandwidth and Encoding Scheme Effects on Match Filtering	47
4.5 Bandwidth and Encoding Scheme Effects on STAP	50
4.6 Computational Resources	58
V. Conclusion	60
5.1 Overview	60
5.2 Research Goal	60
5.3 Results and Contribution	60
5.4 Future Research	61
Bibliography	63

List of Figures

Figure	Page
2.1. Example window function and corresponding frequency domain.	6
2.2. LTE frequency domain structure of one symbol.....	7
2.3. LTE time domain structure of one radio frame.	8
2.4. LTE resource grid.	10
2.5. Example 64-ary QAM encoding scheme.	11
2.6. Match filtered response for a basic LFM.....	13
2.7. Match filtered response for 20MHz LTE symbol.	14
2.8. Uniform pulse versus pulse diverse Doppler processed LTE.....	17
2.9. Clutter Doppler spreading due to pulse diversity.....	18
2.10. Datacube for a one element ULA, showing dimensions over which radar signals are processed.	19
2.11. STAP datacube showing dimensions over which radar signals are processed.....	20
2.12. Array geometry key parameters.	21
2.13. PBR Doppler geometry key parameters.	27
3.1. MATLAB LTE Toolbox resource grid for one radio frame.....	29
3.2. MATLAB LTE downlink channel GUI.	30
3.3. Example code to generate LTE signals with MATLAB Toolbox.....	31
3.4. AFIT Toolbox resource grid for one radio frame.	31
3.5. Example code to generate LTE signals with AFIT Toolbox.....	32
3.6. Time and frequency domain of one simulated pulse.	34

Figure	Page
3.7. Receiver, transmitter, and range/azimuth CUT locations in 3-dimensional coordinates.	37
4.1. Match filtered CPI using LTE signal.	42
4.2. Doppler processed CPI using LTE signal.	43
4.3. 100 match filtered LTE pulses with uniform randomly varying bandwidth.	46
4.4. 100 Doppler processed LTE pulses with uniform randomly varying bandwidth.	46
4.5. Variance of 400 realizations of match filtered LTE pulses with uniform randomly varying bandwidth.	46
4.6. Variance of 400 realizations of Doppler processed LTE pulses with uniform randomly varying bandwidth.	46
4.7. Match filtered variance for each LTE mode.	48
4.8. Variance of 200 realizations of match filtered QPSK LTEs.	49
4.9. Mean and standard deviation of 200 SINR curve realizations.	51
4.10. Mean SINR_L curves for the LTE 10MHz mode: short vs long filter length.	52
4.11. Mean SINR_L curves for the 16QAM LTE: short vs long filter length.	52
4.12. Mean SINR_L curves with and without CP for each LTE mode.	55
4.13. Mean SINR_L curves with and without CP for each encoding scheme; 1.4-5 MHz modes.	56
4.14. Mean SINR_L curves with and without CP for each encoding scheme; 10-20 MHz modes.	57

List of Tables

Table		Page
2.1.	LTE modes samples per symbol, useful samples, and sample rate.....	9

List of Abbreviations

AFIT	Air Force Institute of Technology
AWGN	additive white Gaussian noise
BW	bandwidth
CDS	clutter Doppler spread
CMT	covariance matrix taper
CP	cyclic prefix
CPI	coherent processing interval
CNR	clutter to noise ratio
CSRE	cell specific reference element
CUT	cell under test
DOF	degrees of freedom
ECG	extended constant gamma
FDD	frequency division duplexing
FFT	fast Fourier transform
GMTI	ground moving target indication
i.i.d.	independent identically distributed
IPOP	in-plane out-of-plane
LFM	Linear Frequency Modulated
LTE	long term evolution
MF	matched filter
MBSFN	multicast broadcast single-frequency network
NFFT	number of FFT samples
OFDM	orthogonal frequency division multiplexing
PBR	passive bistatic radar

PRI	pulse repetition interval
PRF	pulse repetition frequency
QAM	quadrature amplitude modulation
QPSK	quadrature phase shift keying
RCS	radar cross-section
SINR	signal to interference-plus-noise ratio
SNR	signal to noise ratio
STAP	space-time adaptive processing
TDD	time division duplexing
ULA	uniform linear array
USAF	United States Air Force

ORTHOGONAL FREQUENCY DIVISION MULTIPLEXED WAVEFORM
EFFECTS ON PASSIVE BISTATIC RADAR

I. Introduction

1.1 Problem Description

Communications waveforms act as signals of opportunity for passive bistatic radars (PBRs) ground moving target indication (GMTI). However, these signals of opportunity have high range sidelobes and pulse-diverse waveform aspects which degrades range-Doppler processing. These and other characteristics of communications waveforms drive PBR performance. A PBR will process uncooperative waveforms, and thus the radar performance is largely dependent on the properties of the available waveform.

1.2 Research Motivation

Increasing demand for wireless communication and dwindling spectrum availability has encouraged the spread of orthogonal frequency division multiplexing (OFDM) to increase channel capacity. The persistence and abundance of these waveforms and others has led to radars competing for frequency spectrum. PBRs can collect these waveforms and avoid competing for contested and overcrowded spectrum. Since PBR do not transmit, there are advantages such as fewer vulnerabilities to deliberate interference, enhanced difficulty detecting the receiver, and lower hardware costs and weight due to the lack of a transmitter requirement.

1.3 Research Goal

The goal of this research is to characterize the effects of communications waveforms available to space-time adaptive processing (STAP) for PBR GMTI. The research will focus on the long term evolution (LTE) OFDM. The research will provide a performance metric that can be used to compare waveform performance. This performance metric will enable future research in PBR GMTI flight path planning and sensor placement optimization.

1.4 Previous Works

The research described in this thesis is an extension of the work published in [1]. There were no other works were identified that specifically focused on the effects of waveform selection on PBR GMTI performance. However, there are other works with similar research goals, which will be elaborated upon in this section. Other works have analyzed LTE and OFDM waveforms for radar applications such as [2–7].

Evers and Jackson in [2] examine the cross and self ambiguity function for one particular LTE configuration, and focus on cell specific reference element (CSRE)s. In contrast to [2], the research in this thesis focuses on multiple encoding schemes, bandwidth modes, and the user-data portion of the LTE waveform. Additionally, Evers and Jackson in [3] examine the application of LTE waves to synthetic aperture radar. As part of the research in [2,3], Evers crafted an OFDM toolbox for AFIT. This toolbox was utilized in the early stages of the research in this thesis, but eventually transitioned to the MATLAB LTE Toolbox. The usage of each toolbox for this research is outlined in Chapter III. The simulations required an accurate model for LTE OFDMs, and much of the prior works from Evers aided crafting LTE signals. Ultimately the MATLAB toolbox was used for its more accurate LTE signal generator. Establishing an accurate LTE simulation built largely upon [8], which explains the

4-G cell phone signals in careful detail.

Other works have examined waveform diversity in a more general sense [9], and provided insights to some of the challenges facing the PBR community. Works such as [10], introduce new processing techniques to manage sidelobe problems inherent to pulse diverse radar systems. Lastly, works such as [11] test the feasibility of passive moving target detection while varying target type and velocity, but in a set of limited configurations. Additionally, the objective of [11] revolved more around demonstration of the feasibility of using a LTE signal for GMTI with a real cell-tower. The research in [11] will become more applicable should there be a desire to demonstrate GMTI from cell towers or laboratory configurations. The work in [5] develops a Bayesian framework for tracking moving targets and estimating their velocity. The mathematical approach in [5] used to define OFDM is complementary to the research described in this thesis. An overview of the radar range equation parameters and considerations for each in PBR applications using emitters of opportunity such as LTE signals are described in [7] and complementary to this thesis.

Works such as [6] focus on the application of a specific processing technique for airborne PBR with a fixed transmitter and fixed receiver. Klock [6] makes use of the the MATLAB LTE tool box for OFDM pulse generation. Additionally, Klock considers a pulse width on an entire radio frame, which is much longer than the pulse width considered in Chapters III-IV. The conclusions in [6] are limited to correlation analysis used to compare processing gain.

The majority of this research expands upon [4]. Lievsay contributed to the foundations of STAP as detailed by Richards in [12,13] by expanding upon clutter models. This research used a STAP and clutter model developed by Lievsay, and described in [4]. Furthermore, Lievsay expanded on the works of Guerci in [14], by introducing a covariance matrix taper to account for the effects of radar-pulse waveform-diversity.

In addition to the works of Lievsay, much of the preliminary research as described in the Section 2.3 and Sections 4.2-4.5 was built on radar fundamentals from [13, 15].

II. Theory

2.1 Overview

This chapter describes the concepts, definitions, and mathematics necessary to understand the PBR GMTI and STAP modeled in this research. The chapter covers a description of OFDM and LTE waveforms. Next, an introduction to fundamental radar principles used for fast and slow-time dimension data processing is presented. Then, the spatial dimension is included and an overview of STAP, the algorithm used for processing data across space and time, is presented. Lastly, PBR is defined in terms of its geometry, and differences between the monostatic and bistatic cases are explained.

2.2 OFDM and Communication Waveforms

In general, OFDM waveforms consist of signals with data encoded on a set of uniformly spaced subcarrier frequencies. By encoding data on sub-carriers spaced across a channel band, data can be transmitted in parallel, increasing the communication data rate. OFDM waveforms are designed to reduce sub-carrier interference; sub-carrier frequencies are chosen then time-windowed in conjunction with a sample rate to preserve carrier orthogonality (see Figure 2.1). By using the Fourier transform to generate time-domain communication waveforms, OFDM signals may be conveniently defined/encoded in the frequency domain. Each sub-carrier can be defined/encoded independent of other sub-carriers within the OFDM, then summed to generate the complete OFDM. This is important because the LTE signal is defined in the frequency domain by the user data and any signal specific overhead data that will be encoded onto the waveform¹.

¹Signal specific overhead for the LTE will be discussed in subsequent sections, and is illustrated in Figure 2.4.

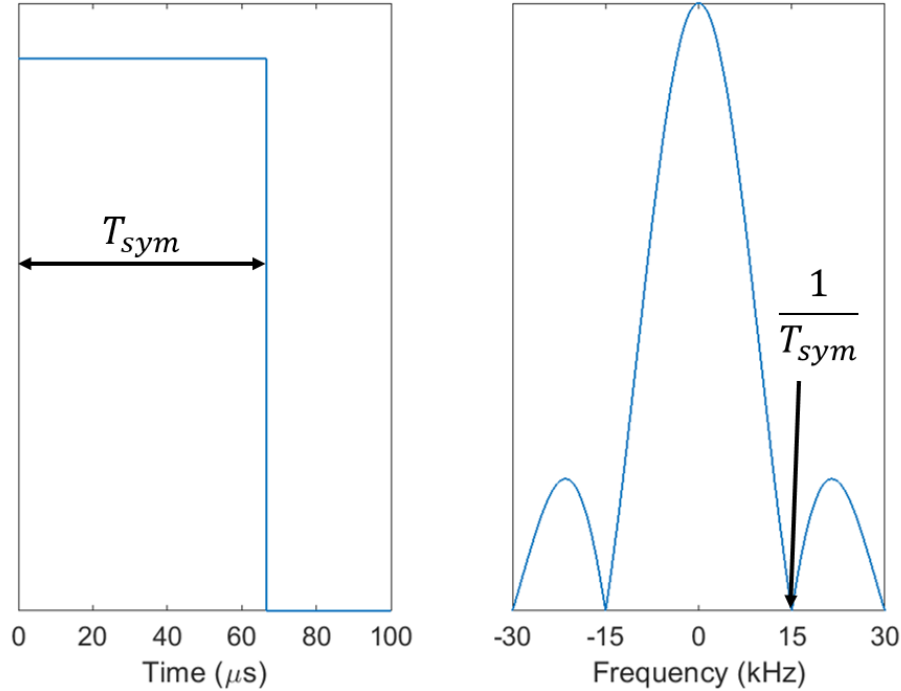


Figure 2.1. A window function and corresponding frequency domain. T_{sym} is the window duration, and represents the duration of one LTE symbol.

Often sub-carriers at the upper and lower end of the sample rate are forbidden, forming guard bands, in order to prevent interference with adjacent frequency bands (see Figure 2.2). Another method of reducing interference requires a guarded time interval. During the guarded time interval, a portion of the transmitted signal is repeated. The LTE OFDM refers to this repeated signal as the cyclic prefix (CP). The CP improves reliability of successful information exchange but also has the effect of creating radar ambiguities [2].

2.2.1 The LTE OFDM.

The LTE waveform, commonly referred to as the 4th generation (4-G) cell phone signal, is a specific application of OFDM. LTE waveform ubiquitous persistence makes it a desirable signal of opportunity. This section will describe the LTE struc-

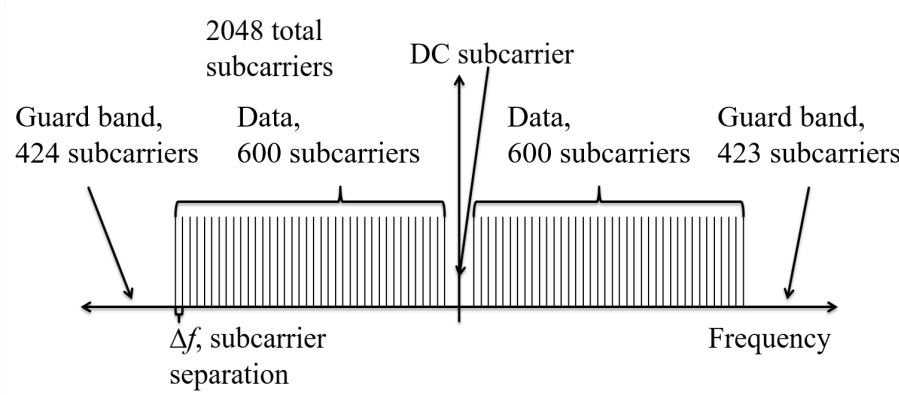


Figure 2.2. This image depicts the frequency domain structure of one symbol, excluding the cyclic prefix, of the LTE 20MHz extended mode. There are 2048 samples of which 1200 samples are data carriers. This Figure is derived from [2] with permission from Dr. Jackson.

ture and properties. The waveform is based on the European Telecommunications Standards Institute (ETSI) specification [16]. The signal is defined in both time and frequency domains. There is an uplink (from mobile device to tower) and a downlink (from tower to mobile device) signal. This research focuses on the downlink signal due to higher power and greater broadcast coverage. The mobile device and tower signal exchange modes are time division duplexing (TDD) and frequency division duplexing (FDD). In the TDD mode, the tower base station transmits a downlink signal followed by an uplink signal listening period. In the FDD mode, the tower base station continuously transmits a downlink signal and listens for an uplink signal on other frequency spectrum. Refer to Figure 2.3 for an image representative of the LTE downlink time domain.

The LTE time domain is designed around a fundamental time-step, T_s , where $T_s = 1/30720000s$. All other time intervals are defined as integer multiples of T_s . For instance, a radio frame is defined as $307200T_s$, or 10 ms, and a subframe is defined as $30720T_s$, or one tenth of one radio frame. Each subframe has two slots where each slot duration is $15360T_s$. The LTE signal can operate in one of two time-domain modes;

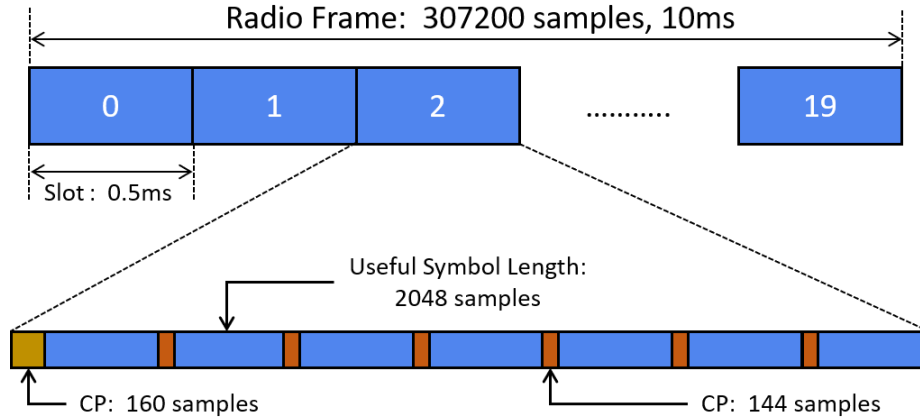


Figure 2.3. This image depicts one LTE 20MHz normal channel mode radio frame. One frame has 20 slots, and one slot has 7 symbols. The 20 MHz channel mode has 2048 useful information samples per symbol, 160 samples for the first cyclic prefix in each slot, and 144 for the remaining 6 symbol cyclic prefixes. Note: there is an extended LTE mode in which the cyclic prefix duration is increased and there are 6 symbols per slot instead of 7. This image is derived from [17].

normal or extended. In the extended mode, each slot consists of 6 symbols whereas the normal mode has 7 symbols per slot. Regardless of the mode, the useful symbol duration remains fixed at $2048T_s$ for all symbols. Only the CP duration is dependent on the operating mode. For the extended mode, the CP duration is fixed at $512T_s$ per symbol. However, in the normal mode, the CP is $160T_s$ in the first symbol and $144T_s$ in the remaining 6 symbols of a slot. Figure 2.3 depicts the 20 MHz mode where the sample rate is defined as, $f_s = 1/T_s$, thereby conveniently allowing the depiction of a normal mode radio subframe slot in terms of the number of samples. For example, the number of samples for the useful symbol duration in the 20 MHz mode is

$$\begin{aligned}
 N_u &= f_s 2048T_s \\
 &= \frac{1}{T_s} 2048T_s \\
 &= 2048.
 \end{aligned} \tag{2.1}$$

Each subcarrier of the LTE OFDM is spaced at 15 kHz intervals across the bandwidth. Guard carriers exist at the lower and upper portions of the spectrum and at DC (center frequency). Figure 2.1 shows that 15 kHz spacing preserves orthogonality, due to subcarrier nulling at 15kHz increments. There is one extra guard carrier for negative frequencies, when examining the spectrum at baseband. Refer to Figure 2.2 for the frequency domain of the 20 MHz mode. It is important to note that each subcarrier has one sample per symbol.

All other bandwidth modes have a similar structure with a varying number of data and guard subcarriers; refer to Table 2.1. There are different proportion of guard carriers for the various modes, resulting in different effective bandwidths for each LTE mode. Table 2.1 considers only the useful data portion of the symbol and excludes the CP. The total number of useful samples is defined as $N_u = N_c + N_g$ where N_c is the number of data carrier samples and N_g is the number of guarded carriers in one symbol, excluding the CP.

Table 2.1. LTE modes samples per symbol, useful samples, and sample rate.

LTE MODE (MHz)	Effective Bandwidth (MHz)	Resource Blocks (Count)	Useful Samples (N_u)	Data Carriers (N_c)	Sample Rate (MHz)
20	18.015	100	2048	1200	30.72
15	13.515	75	2048	900	30.72
10	9.015	50	1024	600	15.36
5	4.515	25	512	300	7.68
3	2.715	15	256	180	3.84
1.4	1.095	6	128	72	1.92

The time and frequency domain of LTE signals can be mapped on a grid. One grid location is referred to as an element and consists of one subcarrier for one OFDM symbol duration. One resource block is defined as 12 subcarriers (at 15kHz spacing) for one slot duration (0.5 ms). Figure 2.4 depicts two consecutive resource blocks. The LTE framework can span the entire 10 ms radio frame. Note in Figure 2.4 there

are repeating reference elements and a control signal. A control signal often occupies elements in the first symbols of a slot and radio frame. Other elements, referred to as CSREs, consume LTE resource element real-estate. Control signals and CSRE elements contain information regarding the structure of the LTE signal and act as sub-carrier and timing pilot signals to improve communications performance. User data may occupy the remaining signal elements.

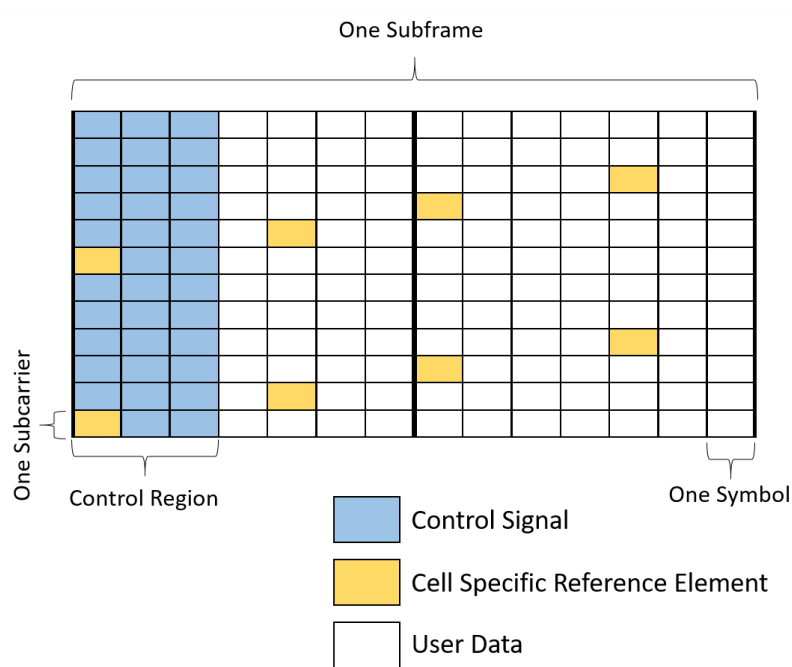


Figure 2.4. This image depicts two consecutive resource blocks. Some of the elements contain LTE signal overhead (colored), other elements contain LTE user data (white).

The user data may be encoded in elements using 64-ary, 16-ary, and quadrature phase shift keying (QPSK) encoding schemes. There are many different encoding schemes used in communication waveforms, but 64-ary, 16-ary, and QPSK are common in LTE signals. Figure 2.5 depicts a common 64-ary constellation used in LTE waveforms to encode user data and CSREs. Larger M-ary encoding schemes enable higher communications bit-rates, but require higher signal to noise ratio (SNR). Communication waveforms, such as the LTE, are designed with the intent of sender/re-

ceiver information exchange. This research focuses on the application of the LTE waveform to PBR, instead of information exchange.

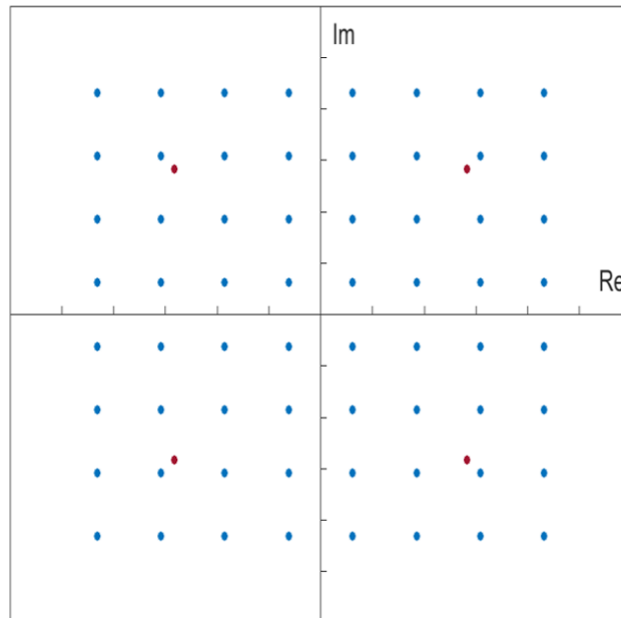


Figure 2.5. This is an example of a standard 64-ary QAM encoding scheme for the subcarriers of a LTE OFDM. Red: CSRE. CSREs are one of four complex values; they do not carry random user data and occur at predictable frequency and time intervals, [3].

2.3 Radar: Fast and Slow-Time

Traditional pulsed monostatic radar systems transmit a waveform for a brief duration, τ , then have a listening period, followed by another transmit duration. This process repeats at a frequency called the pulse repetition frequency (PRF). The total transmit and listen time is referred to as the pulse repetition interval (PRI), and is $1/PRF$. Pulsed radars measure signal delay over fast-time for a single pulse, and phase drift over slow-time for many pulses. Fast-time occurs over the duration of one pulse at the sample frequency of the radar. Slow-time occurs over the duration of many pulses at the PRF of the radar. Pulsed radar fundamentals can serve as a guide

to understanding PBR, and the next two sections will outline fast-time and slow-time radar processing.

2.3.1 Fast-Time.

Instead of decoding the data in a signal, a radar system weights each sample of the received signal to maximize the SNR at a point in time corresponding to the delay of the target [13]. Maximizing the SNR of the received radar waveform is a fundamental goal of radar signal processing. The set of weights applied to the received digital radar waveform that maximizes the SNR is defined as the matched filter. For finite length transmit signals with assumed additive white Gaussian noise, the matched filter becomes the time reversed complex conjugate of the transmitted waveform [13]. The matched filter is convolved with the received signal (this requires knowledge of the transmitted waveform), and can be normalized by the peak value of the convolution.

For this research, a bold lower case character represents a column vector, and a bold capital character represents a matrix. Consider the received digital signal $\mathbf{x} = \mathbf{s} + \mathbf{n}$ where \mathbf{s} is the signal and \mathbf{n} is independent identically distributed (i.i.d.) noise. The SNR is simply the signal power divided by the noise power and for digital signals can be written as [13]

$$\text{SNR} = \frac{\mathbf{w}^H \mathbf{s} \mathbf{s}^H \mathbf{w}}{\mathbf{w}^H \mathbf{R}_n \mathbf{w}}, \quad (2.2)$$

where \mathbf{w} is the set of weights we optimize for the maximum SNR, and \mathbf{R}_n is the noise covariance matrix. If the noise, \mathbf{n} , is modeled as additive white Gaussian noise (AWGN), then the covariance matrix is a diagonal matrix, and $\mathbf{R}_n = \sigma_n^2 \mathbf{I}$: a product of the noise power with the identity matrix. Using the Schwartz inequality, it can be

shown that the maximum SNR is achieved when [13]

$$\mathbf{w} = \eta \mathbf{R}_n^{-1} \mathbf{s}^*, \quad (2.3)$$

where η is any scalar. If the scalar is chosen to be σ_n^2 then,

$$\mathbf{w} = \mathbf{I} \mathbf{s}^* = \mathbf{s}^*, \quad (2.4)$$

and the optimum filter weights, \mathbf{w} , are then given as the complex conjugate of the signal, \mathbf{s} . A simple rectangular-time-windowed Linear Frequency Modulated (LFM) waveform will have a match filtered response as depicted in Figure 2.6.

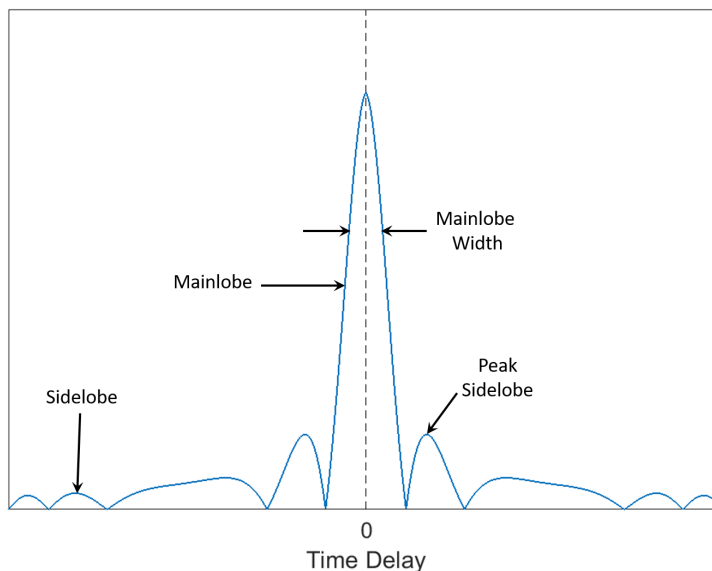


Figure 2.6. Match filtered response for basic LFM that includes mainlobe and sidelobes [18].

In general, match filtered OFDM communication waveforms such as the LTE have wider main lobes and higher sidelobes when compared to traditional radar-specific waveforms. Additionally, communication waveforms often have cyclic or redundant pieces appended to the signal beginning or end. This creates high match filtered

responses distant from zero-delay, which increases likelihood of range-mismatch; refer to Figure 2.7. Note the maximum magnitude of the lag range in Figure 2.7 is around 20km (this will be important when choosing τ for PBR).

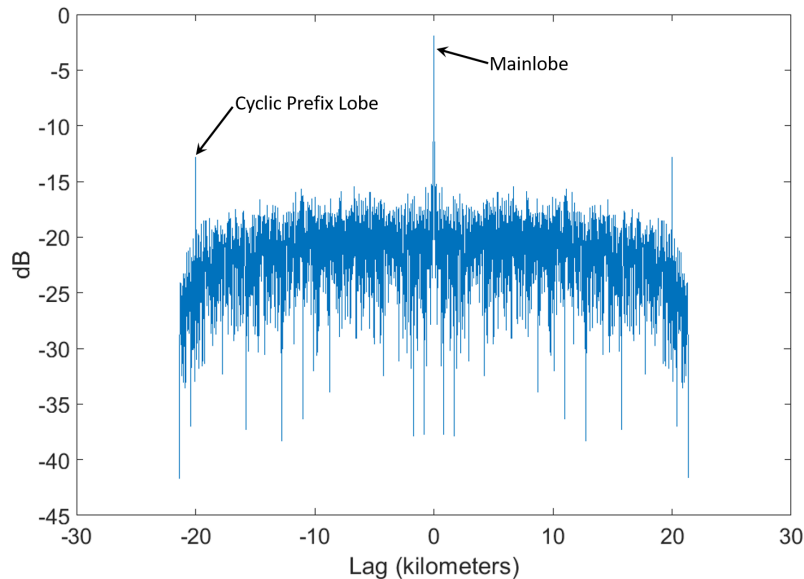


Figure 2.7. Match filtered response for one full 20MHz LTE symbol, including the cyclic prefix. The time-delay can be interpreted in terms of a lag distance. This Figure is not intended to depict range resolution; the mainlobe sample lag must be examined more closely and the bistatic collection geometry must be considered.

Examining the match filter output, such as in Figure 2.6, the main lobe has a particular width. The width of this main lobe indicates the best achievable radar resolution of the waveform; narrower mainlobes achieving better range resolution. For monostatic radars, the approximate relationship is expressed as [13]

$$\Delta R \approx \frac{c}{2B}, \quad (2.5)$$

where increasing the waveform bandwidth, B , improves the achievable resolution.

2.3.2 Slow-Time.

In order to understand pulsed radar slow-time processing it is useful to first understand the basic concept of Doppler shift. A wavefront is compressed or stretched when it reflects off an object moving in the direction of the wave propagation. We express this effect in a simple form,

$$f_r = f_t + f_d, \quad (2.6)$$

where f_r is the received frequency, f_t is the transmitted frequency, and f_d is the Doppler frequency. The Doppler frequency, f_d , is positive for an ingressing target and negative for an egressing target. Let us now examine how to find f_d and see how it relates to the velocity of a moving object so that when given f_r we can predict the velocity of a moving object or predict f_r when given the velocity of an object.

In radar signal processing, it is useful to predict the Doppler frequency to draw conclusions about the velocity of the target. The Doppler shift, f_d , is related to the rate of change of the phase of the received signal. For a monostatic radar, f_d is calculated as

$$\begin{aligned} f_d &= \frac{-2f_t}{c} \bar{v} \cdot \hat{k}, \\ &= \frac{-2\bar{v} \cdot \hat{k}}{\lambda}, \end{aligned} \quad (2.7)$$

where λ is the signal wavelength (typically based upon the carrier wavelength), \bar{v} is the velocity vector of the reflector, and \hat{k} is the unit vector pointing in the direction of the target. Using Fourier properties it can then be shown that the received signal model is the product of a delayed copy of the transmitted signal and a complex

exponential [19],

$$s_r(t) = s_t(t - \kappa)e^{j2\pi f_d(t-\kappa)}, \quad (2.8)$$

where t is time and κ is the time delay.

The Doppler induced by typical ground moving targets is minimal, but the accumulated change in phase over slow-time is more detectable. Examining this accumulated phase change in pulsed radars is called Doppler processing. Doppler processing is simplified in the case where PRI is constant; which is not necessarily the case for non-cooperative passive bistatic radars. For a constant PRI, Doppler processing is implemented with a Fourier transform across slow-time samples, while a staggered PRI requires additional temporal accounting.

Eventually phase change accumulated between adjacent pulses may approach π or $-\pi$ radians, beyond which the accumulated phase becomes ambiguous. For a properly chosen PRI, it can be assumed that Doppler shifts fall within the lowest non-ambiguous velocity range. Often it is convenient to describe Doppler shift in terms of normalized Doppler, \bar{f}_d , which ranges from -1/2 to 1/2 cycles per sample. Normalized Doppler can be related to the Doppler frequency through the radar PRF,

$$\bar{f}_d(PRF) = f_d = \frac{2\bar{v} \cdot \hat{k}}{\lambda}, \quad (2.9)$$

and then the Doppler frequency can be related back to the target velocity using (2.7).

The total interval over which slow-time samples are aggregated is called the coherent processing interval (CPI), and is typically given in terms of the number of pulses contained by the CPI rather than the duration of time. Assuming a fixed PRI, increasing the number of samples aggregated across slow-time improves Doppler

resolution. Doppler resolution can be described as,

$$\Delta f_d = \frac{PRF}{M}, \quad (2.10)$$

where M is the number of slow-time transmitted pulses. Some monostatic radars transmit a unique signal each pulse. In pulse diverse systems the interference floor is increased and the Doppler energy is spread across slow time. Figures 2.8-2.9 depict the Doppler spread, and are depicted here to illustrate the spreading effect which is accounted for with a taper when simulating STAP [4].

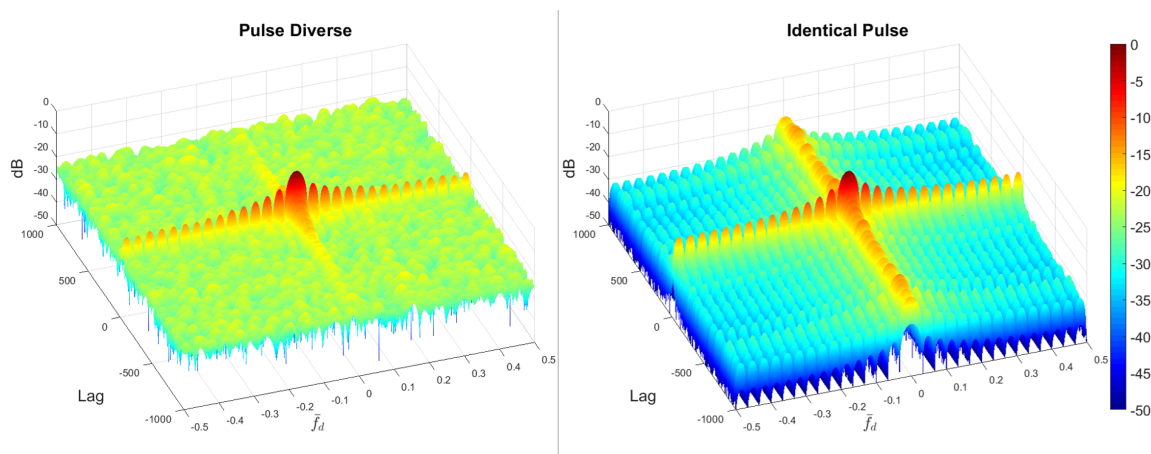


Figure 2.8. Doppler processing comparison for target response at zero-lag zero Doppler. The coherence across fast time (lag) and Doppler visible with identical pulses (right) is smeared with pulse diversity (left). The noise floor is also raised with pulse diversity [4]. The CPI on the left and right is a 30 pulse train of 20 MHz LTE waveforms, however the pulse diverse CPI has unique random user data in each pulse, and the identical pulse CPI has pulses with identically encoded data. The pulses are match filtered then a Fourier transform is applied across slow-time.

2.4 Space-time Adaptive Processing

Pulsed array radars enable processing in spatial dimensions. The discussion on pulsed radars in the previous section was limited to two temporal dimensions: fast and slow-time. With the addition of an array, pulsed radars can detect targets over fast-

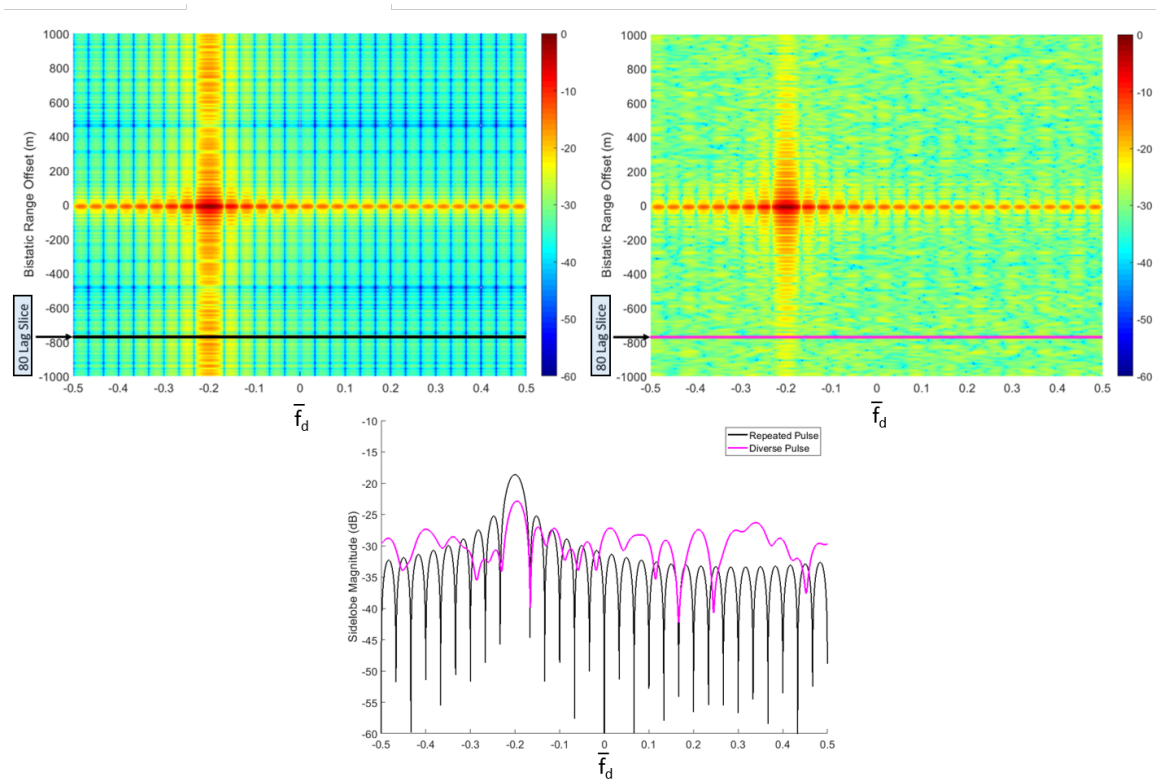


Figure 2.9. Fixed or repeated pulse (top left) versus diverse pulse (top right) clutter Doppler spread. The slice of all samples at the 80th lag (bottom).

time, slow-time, and the additional spatial dimensions. A planar array has two spatial dimensions, and a uniform linear array (ULA) is limited to one spatial dimension. The one spatial and two temporal dimensions of a ULA lend themselves to conceptualizing STAP with a data cube. A one-element ULA can be depicted as a matrix (see Figure 2.10), and for a multi-element ULA see Figure 2.11.

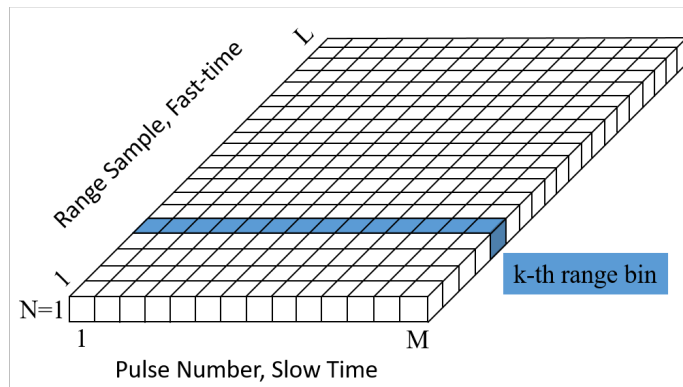


Figure 2.10. Datacube for a one element ULA, showing dimensions over which radar signals are processed [13]. The length of the fast time dimension, L , is the match filter length.

With the data cube conceptualization, each sample of the match filtered signal is stored in one cell and the set of all samples for one particular range (or lag) is referred to as the space-time snapshot, χ_k , where the subscript, k , is the k -th particular range bin. When samples are visualized as a data cube, the set of all samples for one particular range are arranged as a matrix, as depicted by the range cell under test (CUT) in Figure 2.11. In order to process the range CUT, the cells of the matrix are re-arranged into a single column vector, χ_k . The arrangement of the column vector, χ_k , is the same the MATLAB colon operator used to convert a matrix to column vector. For example, if \mathbf{A} is a $N \times M$ matrix in the MATLAB workspace, then $\mathbf{A}(:)$ is a $NM \times 1$ column vector. The spacetime snapshot can be broken into its component pieces [4],

$$\chi_k = \chi_{c_k} + \chi_{n_k} + \chi_{t_k}, \quad (2.11)$$

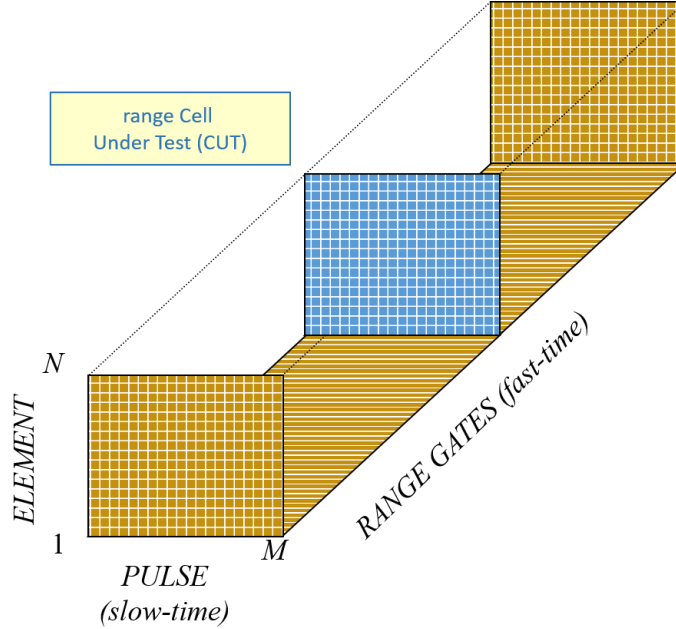


Figure 2.11. Datacube showing the dimensions over which radar signals are processed [13]. This cube has N elements, whereas Figure 2.10 has one element. STAP fixes a particular range cell under test then performs processing across the remaining two dimensions.

where χ_{c_k} is the clutter contribution, χ_{n_k} is the noise contribution, and χ_{t_k} is the target contribution. The clutter model and noise used for this research is expanded upon in Section 3.4.2. In order to focus on the waveform effects in the clutter environment, the contribution from a target is considered $\mathbf{0}_{NM \times 1}$ for this research.

STAP algorithms fix a range CUT then perform processing across the remaining two dimensions. Filters are typically trained from adjacent data cube range cells when a clairvoyant model is not assumed. In Section 2.3.2 normalized Doppler was introduced. Now with the addition of the spatial dimension, normalized spatial frequency, ϑ , is introduced. Consider a side-looking array configuration as depicted in Figure 2.12.

Now consider a response arriving at the elevation and azimuth angles, θ and ϕ respectively, and measured by N array channels. The spatial frequency observed by

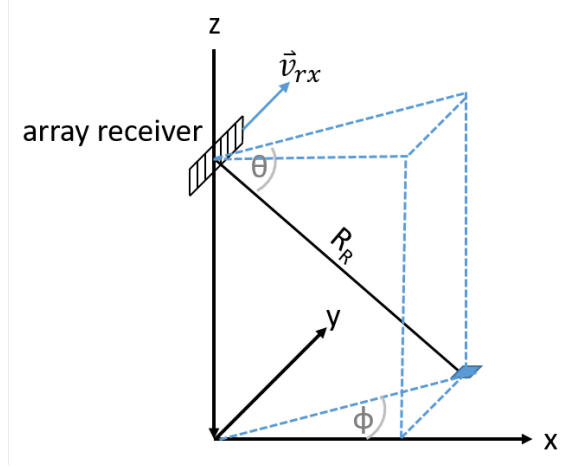


Figure 2.12. Array and platform geometry for arbitrary target. θ is the elevation angle, ϕ is the azimuth angle, and R_R is the range from the array center to the ground patch of interest.

the array is given by [12, 15],

$$\vartheta = \frac{d}{\lambda} \cos(\theta) \sin(\phi), \quad (2.12)$$

where d is the channel spacing along the x-axis, and λ is the carrier wavelength. The spatial steering vector for N channels is discussed later in (2.20).

In Section 2.3.1, it was shown that the filter which maximizes SNR is the conjugate of the transmitted signal (2.4), implemented with a correlation. Similar to fast-time range data processing, space-time processing is the application of a set of weights to the space-time observations. Expanding upon the set of weights described in Section 2.3.1, the set of weights used for STAP, \mathbf{w}_k , vary over normalized spatial (ϑ) and Doppler (\bar{f}_d) frequencies. Applying \mathbf{w}_k to the vectorized space-time data, $\boldsymbol{\chi}_k$, yields the test statistic, \mathbf{y}_k , and is given as,

$$\mathbf{y}_k(\vartheta, \bar{f}_d) = \mathbf{w}_k^H \boldsymbol{\chi}_k, \quad (2.13)$$

where k designates the k -th range bin (also referred to as the current range CUT as shown in Figure 2.11) and \mathbf{H} is the Hermitian of \mathbf{w}_k . It is well known that the optimum weight is [20],

$$\mathbf{w}_k(\vartheta, \bar{f}_d) = \eta \mathbf{R}_k^{-1} \mathbf{v}(\vartheta, \bar{f}_d), \quad (2.14)$$

where \mathbf{v} the space-time steering vector, \mathbf{R}_k is the interference covariance matrix, and η is an arbitrary scale factor. The set of weights for fast-time processing, (2.3), is similar to the set of weights for STAP, (2.14), except with STAP a space-time steering vector replaces \mathbf{s} , and the interference covariance matrix depends on space. Clutter is therefore coherent over space and time. The space-time steering vector matches to a constant change in phase from channel to channel and pulse to pulse. The clutter covariance matrix for STAP must characterize clutter correlation over space and time. In order to model the de-correlation over slow-time due to pulse diversity (recall that communication waveforms are pulse diverse from embedded random user data), a covariance matrix taper (CMT) can be used [4, 14]. The taper models the pulse-dependent distributed contributions over range (or fast-time), and pulse-to-pulse variation across slow-time [4]. It has been shown that pulse diverse waveforms cause clutter Doppler spreading, [4, 21], as was illustrated in Figure 2.8. The taper is applied as follows,

$$\mathbf{R}_k = \int \mathbf{T}(\kappa - \kappa_o) \odot \mathbf{R}(\kappa) d\kappa, \quad (2.15)$$

where \odot is the Hadamard product (element or piece-wise product), and κ_o is the peak correlation located at the range CUT, and $\mathbf{R}(\kappa)$ is the clutter covariance matrix

$$\mathbf{R}(\kappa) = \mathbf{E} [\boldsymbol{\chi}_{c_k} \boldsymbol{\chi}_{c_k}^H], \quad (2.16)$$

where $\boldsymbol{\chi}_{c_k}$ is the clutter space-time snapshot at the k -th range and is discussed further in Section 3.4.2. The full derivation and context for the taper, \mathbf{T} , is in [4] but a

synopsis is as follows. Define

$$\mathbf{t}(\kappa) = \begin{bmatrix} R_{xx}^1(\kappa) \\ R_{xx}^2(\kappa) \\ \vdots \\ R_{xx}^M(\kappa) \end{bmatrix}, \quad (2.17)$$

where $R_{xx}^m(\kappa)$ is the normalized autocorrelation of the m -th pulse, and M is the total number of pulses in the CPI. Then the taper is [4]

$$\mathbf{T}(\kappa - \kappa_o) = \mathbf{t}(\kappa - \kappa_o) \mathbf{t}^H(\kappa - \kappa_o) \otimes \mathbf{1}^{N \times N}, \quad (2.18)$$

where \otimes is the Kronecker product and N is the total number of ULA elements.

Next, the space-time steering vector, \mathbf{v} , is defined as

$$\mathbf{v}(\vartheta, \bar{f}_d) = \mathbf{b}(\bar{f}_d) \otimes \mathbf{a}(\vartheta), \quad (2.19)$$

where \mathbf{b} and \mathbf{a} are the temporal and spatial steering vectors respectively. If we assume a constant PRI and ULA, then the spatial and temporal steering vectors are defined as,

$$\mathbf{a}(\vartheta) = [1 \quad e^{j2\pi\vartheta} \quad \dots \quad e^{j2\pi(N-1)\vartheta}], \quad (2.20)$$

$$\mathbf{b}(\bar{f}_d) = [1 \quad e^{j2\pi\bar{f}_d} \quad \dots \quad e^{j2\pi(M-1)\bar{f}_d}], \quad (2.21)$$

which are only valid if it is assumed that the receiver is a ULA, with evenly spaced receiver elements, and LTE waveform symbols are received at a uniform spacing thereby creating a constant PRI. The spatial and temporal steering vectors could be redefined to accommodate other array geometries or pulse timing.

Finally, the signal to interference-plus-noise ratio (SINR) can be calculated as the ratio of the power of the signal and the power of the interference,

$$\text{SINR} = \frac{P_S}{P_I} = \sigma_s^2 \frac{|\mathbf{w}_k^H \mathbf{v}|^2}{\mathbf{w}_k^H \mathbf{R}_k \mathbf{w}_k}, \quad (2.22)$$

where σ_s^2 is the signal power received at one channel from one pulse. The optimal SINR, denoted as SINR_o , is found by substituting (2.14) into (2.22), which yields,

$$\text{SINR}_o = \sigma_s^2 \mathbf{v}^H \mathbf{R}_k^{-1} \mathbf{v}, \quad (2.23)$$

Equation (2.23) provides an expression for the SINR_o , which depends on the values of the interference covariance, \mathbf{R}_k , and ultimately the signal waveform. SINR loss, which can be denoted SINR_L is given by the ratio of the optimal SINR with the SNR, [22], and is a function of the spatial and Doppler frequencies.

$$\text{SINR}_L = \frac{\text{SINR}_o}{\text{SNR}} = \frac{\text{SINR}_o}{\frac{\sigma_s^2}{\sigma_n^2} NM}, \quad (2.24)$$

where N is the number of array channels and M is the number of slow-time pulses. This metric is used to analyze pulsed radar waveform performance and is the primary metric used in Section IV to evaluate LTE signals used for PBR.

2.5 Clutter Ridge

Transmitter and receiver motion induces a very special structure to the clutter due to the dependence of the Doppler frequency on angle. Assuming half-wave-length channel spacing, an immobile transmitter, and receiver velocity is aligned with array orientation, which is the case for a side-looking array, it is shown in [23] that the

clutter is located along a ridge in angle-Doppler space with a slope, α , defined by,

$$\alpha = \frac{2v_{rx}}{\lambda(PRF)} \quad (2.25)$$

where v_{rx} is the receiver speed, and λ is the carrier wavelength. This is modified to accommodate PBR whereas [23] assumes a monostatic radar. The bistatic slope is half the monostatic case.

2.6 Passive Bistatic Radar

Bistatic radar is a more general scenario than monostatic radar. In the monostatic case, the transmitter and receiver are co-located. In the bistatic case, the transmitter, target, and receiver may have different positions, and the relative geometry of these positions must be considered.

For PBR the Doppler effect must be handled separately for each wavefront interaction. There are two wavefront interactions of concern: transmitter to target, and target to receiver. The transmitter-target relative geometry/motion determines the initial Doppler shift, then the wavefront is re-transmitted from the target toward the receiver, and the relative target-receiver geometry/motion determines the final Doppler shift. The mathematical relationship is described by [4]

$$\begin{aligned} f_{tgt} &= \frac{\hat{k}_{tx} \cdot \bar{v}_{tgt} + \hat{k}_{rx} \cdot \bar{v}_{tgt}}{\lambda}, \\ &= \frac{v_{tgt}}{\lambda} [\cos(\delta - \beta/2) + \cos(\delta + \beta/2)], \\ &= \frac{2v_{tgt}}{\lambda} \cos \delta \cos \frac{\beta}{2}, \end{aligned} \quad (2.26)$$

where \hat{k}_{tx} and \hat{k}_{rx} are unit vectors pointing from the target to the transmitter and receiver respectively, λ is the carrier signal wavelength, β is the bistatic angle, and

δ is the angle between the bistatic angle bisector and target velocity vector. The two-dimensional general PBR geometry is depicted in Figure 2.13 and can easily be extended to three dimensions. The normalized Doppler induced by a target is then

$$\bar{f}_{tgt} = \frac{2v_{tgt}}{\lambda PRF} \cos \delta \cos \frac{\beta}{2}. \quad (2.27)$$

The Doppler induced by the transmitter and receiver is

$$\bar{f}_{tx,rx} = \frac{\hat{k}_{rx} \cdot \bar{v}_{rx} + \hat{k}_{tx} \cdot \bar{v}_{tx}}{\lambda}. \quad (2.28)$$

Assuming PBR, the transmitter is fixed with no motion; thus, we drop the transmitter component and are left with

$$\begin{aligned} \bar{f}_{rx} &= \frac{\hat{k}_{rx} \cdot \bar{v}_{rx}}{\lambda PRF}, \\ &= \frac{v_{rx}}{\lambda PRF} \cos \theta \sin \phi, \end{aligned} \quad (2.29)$$

where θ is the elevation angle and ϕ is the azimuth angle. The PBR geometry is elaborated upon in Section 3.4.1 and Figure 3.7. The total Doppler is,

$$\bar{f}_{tot} = \bar{f}_{rx} + \bar{f}_{tgt}. \quad (2.30)$$

In addition to the Doppler shift, PBR resolution is slightly different. Traditional monostatic resolution is a specific case given by the more general PBR relationship [24]

$$\Delta R \approx \frac{c}{2B \cos(\beta/2)}. \quad (2.31)$$

The next chapter outlines the simulation methodology, process, and assumptions. The theory in this chapter provides the necessary support. This chapter began with

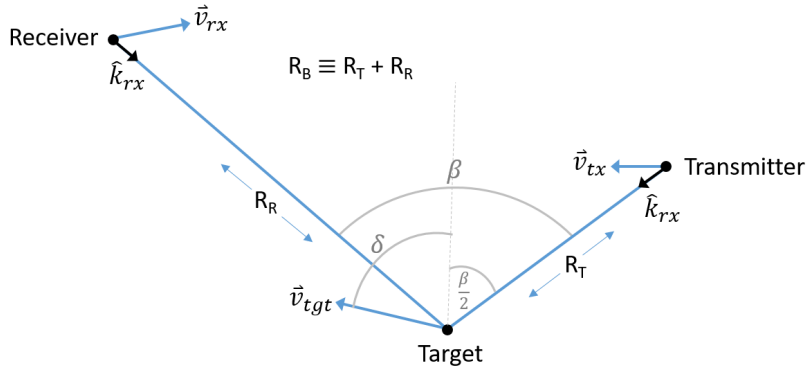


Figure 2.13. PBR Doppler geometry. β is the bistatic angle and δ is the angle between the bistatic bisector and target velocity vector. R_B is the bistatic range.

a description of OFDM communication waveforms and relevant details of the LTE OFDM. The LTE communication signal will be simulated in a radar application, thus an overview of pulsed radar fundamentals was provided. In order to utilize communications waveforms for GMTI, we use a uniform linear array and perform STAP. This requires selecting a PBR geometry.

III. Methodology

3.1 Overview

This chapter provides elaboration on the simulation methodologies. It begins with a description of how the OFDM waveforms were digitally generated, and lists the key waveform parameters of concern. Radar processing techniques such as match filtering, Doppler processing, and STAP, were applied to the digital OFDM waveforms. Lastly, multiple assumptions made for each simulation/experiment are explained.

3.2 Generating the OFDM

Since the primary purpose of this research is a waveform analysis, it is important to understand how to reproduce them. It is also important to know what waveform generation choices were made and why. This section will describe how the digital waveforms were generated and the tools used.

The LTE waveforms were generated primarily using the MATLAB LTE System Toolbox. There is an AFIT Passive Radar Toolbox capable of generating LTE waveforms which has minor limitations to conveniently simulating LTE waveforms, but each generates waveforms valid for research. The MATLAB toolbox simulates the structure of LTE radio frames; including control sequences that contain information related to the structure of the LTE. Figure 3.1 accurately depicts a typical 10 MHz LTE structure and notes three particular control regions of concern. The control region indicated by ‘C’, is referred to as the multicast broadcast single-frequency network (MBSFN), and is used to initialize the transmission of identical data to multiple users simultaneously. For instance, a large number of users may simultaneously stream the same live video [8]. In this instance, the MBSFN control region may occur at long intervals (radio frame or more), and this is a consideration for PBR waveform

utilization, but not explored in further details in this research.

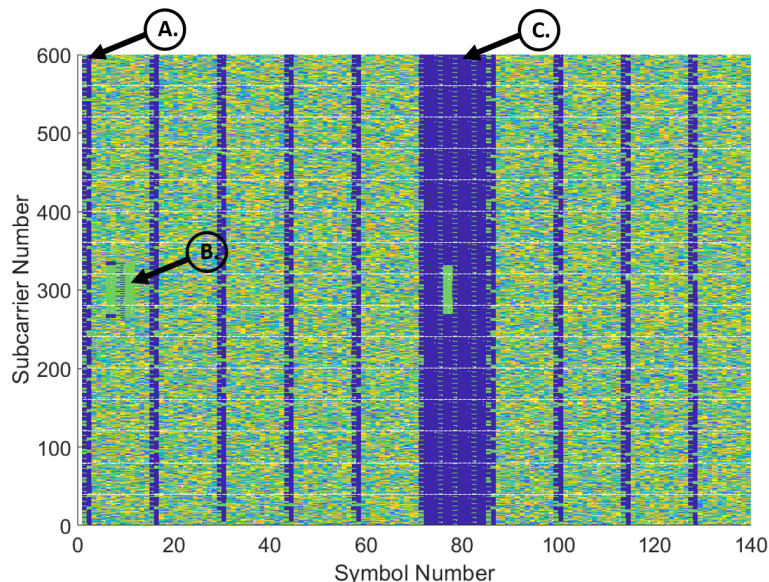


Figure 3.1. The physical layer structure of one LTE radio frame of the 10 MHz mode generated via the MATLAB LTE Toolbox. The overall control structure repeats each radio frame. The color of each cell is only intended to represent the complex data encoded on the subcarrier; blue regions have no data. A: a control signal that repeats the first two symbols of each slot (a slot is 14 symbols). B: a control signal starting on the sixth symbol and centered at the carrier frequency that repeats once each radio frame. C: a control signal and quiet region that repeats mid-frame once each radio frame.

Two parameters examined in this research are the bandwidth mode and encoding scheme. Different LTE bandwidth modes have differing numbers of subcarriers (the vertical axis of Figure 3.1). Increasing the encoding constellation increases the number of possible complex values assigned to the physical layer user data. In order to simulate a LTE radio frame, there are a number of parameters to consider; however, most only affect the control region structure. Refer to Figure 3.2 to see what parameters can be adjusted. The parameters that matter most to this research are a small subset of those available, especially since most parameters affect signal energy in the control region only. The control region effects on PBR phenomena, such as ambiguity, have been investigated by Jackson and Evers in [2].

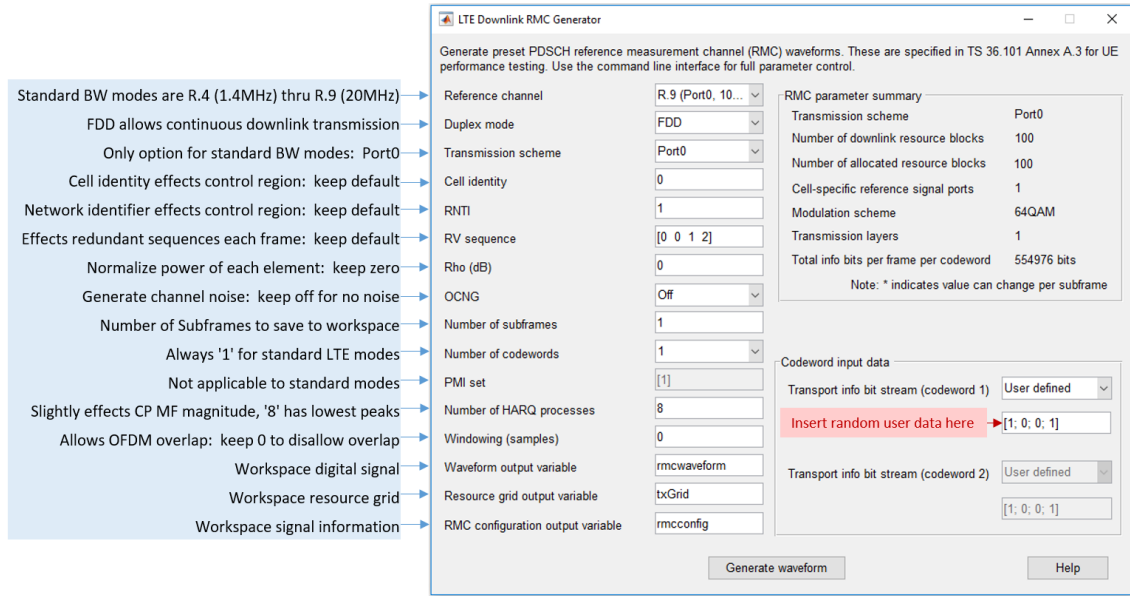


Figure 3.2. MATLAB LTE downlink channel signal generator graphical user interface accompanied with clarifying comments.

It is more convenient to generate signals via commands, and may be done so by following the format of the MATLAB code snippet in Figure 3.3. The MATLAB tool accepts a vector of random bits as an input and will encode the vector onto the LTE signal until the commanded number of radio frames are created. If the data cannot be encoded with the commanded number of radio frames, then the random user data is truncated. If the commanded number of radio frames is longer than required to transmit the random user data, then the random user data is repeated. For this research, the random user data was not repeated.

The AFIT Toolbox LTE generator creates extended mode LTE waveforms (the extended mode has 6 symbols per slot instead of 7 and each cyclic prefix is $512T_s$). The LTE resource grid generated by the AFIT Toolbox has fewer control regions typically present in each LTE slot. An example resource grid is depicted in Figure 3.4. The AFIT Toolbox also has an OFDM generator. The AFIT tool can vary the LTE bandwidth by specifying the number of subcarriers. It may be possible to use the

```

1 - rc = 'R.9';
2 - rmc = lteRMCDL(rc);
3 - rmc.DuplexMode = 'FDD';
4 - rmc.TotSubframes = 20;
5 - rmc.PDSCH.Modulation = '64QAM';
6 - userData = randi([0 1],1e6,1);
7 - [Signal,Grid,SigInfo] = lteRMCDLTool(rmc,userData);

```

Figure 3.3. This code will generate 2 radio frames of a 20MHz Mode 64QAM FDD LTE normal mode downlink signal with random user data on non-control elements. The MATLAB LTE Toolbox must be installed.

OFDM generator to vary LTE bandwidth modes, control regions, encoding schemes, etcetera, but for this research the AFIT OFDM generator was not used.

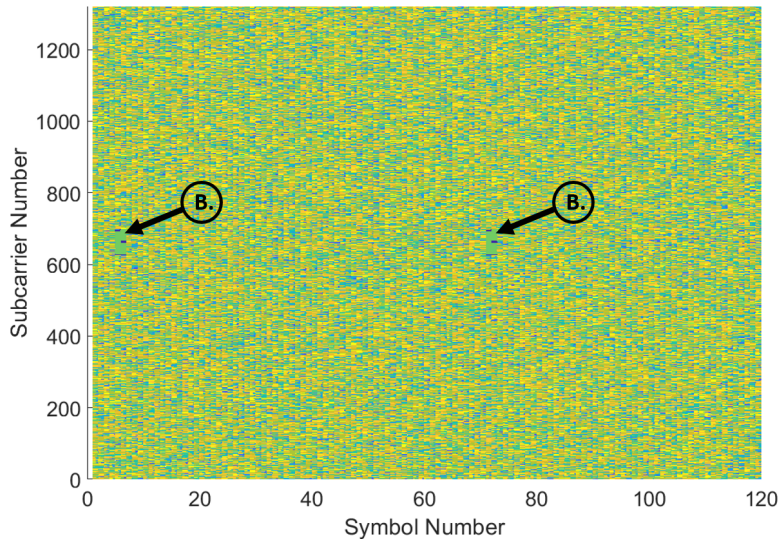


Figure 3.4. This is the physical layer structure of one radio frame of the 20MHz mode generated via the AFIT Toolbox. The color of each cell is only intended to represent the complex data encoded on the subcarrier; blue regions have no data. B: a control signal starting on the fifth symbol and centered at the carrier frequency that repeats each half-radio frame. The control signal in this image is labeled B. since it is similar in function to the control signal generated by the MATLAB Toolbox as seen in Figure 3.1.

Using the AFIT tool, random user data is generated for each workspace information object. This is slightly different than the MATLAB tool, which generates a signal, including new random user data, from an information object. Thus, many

random signal realizations may be created from one MATLAB tool signal information object. In contrast, a new signal information object must be created for each realization when using the AFIT tool. More details regarding the AFIT tool are accessed via toolbox help files located in the AFIT Passive Radar Toolbox directory. The resource grids generated by the AFIT tool and the MATLAB tool may be compared by examining the workspace signal information objects. Example MATLAB and AFIT resource grids may be compared in Figures 3.1 and 3.4.

```
1 txInfo = lte('n_sym',120);  
2 [txSig, t] = txInfo.generateBasebandSignal;
```

Figure 3.5. This code will generate 1 radio frame of a 20MHz Mode 64QAM FDD LTE extended mode downlink signal with random user data on non-control elements. The AFIT Passive Radar Toolbox must be in the current path.

Simulating LTE waveforms can be difficult, given the waveform flexibility. This section detailed how LTE waveforms were created. There are differences between the AFIT and MATLAB tools, but each generates waveforms valid for research. The MATLAB tool was used to generate waveforms for the results in Chapter IV. The next sections describe how the digitally generated LTE signals were tailored for application to radar simulations.

3.3 Radar Model Assumptions

This section explains assumptions made for match filtering and Doppler processing (fast and slow-time processing) experiments. In an effort to focus on fast and slow-time processing waveform effects, experiments assumed a fixed transmitter, fixed receiver, no propagation losses, and normalized AWGN of 1 Watt. A 3-dimensional antenna pattern was assumed for the transmitter and receiver; important for modeling the power received by each clutter patch. The antenna transmitter and receiver

gain models from [4] were used. The receiver main lobe was set to 0° azimuth, and the transmitter yaw was set to 0° placing the main beam pointing toward the range-azimuth CUT. Section 3.3.1 and 3.3.2 focus on the reasoning behind two fundamentally important radar model assumptions.

3.3.1 Symbol Extraction.

Radar signal experiments were conducted using digitally generated LTE waveforms. This section will explain the simulation choices and assumptions for the PRI and CPI. First, symbols were extracted from the radio frame structure in order to focus data analysis conclusions to the symbols, rather than the overarching LTE structure and control regions. This is important to note, because pulsed radars process signals based on specifically designed PRIs, CPIs, and ideal waveforms. For PBR the PRI and CPI must be carefully chosen, because performance will vary depending on what portion of the LTE radio frames are used. Thus, for this research an arbitrary fixed PRI is assumed (the PRI does not need to be a fixed interval, but it simplifies the simulation by enabling use of the fast Fourier transform (FFT)). Additionally, for many of the experiments the LTE waveform exclusively used the structure of the fifth symbol on the resource grid for each radar pulse. This removed control regions in order to focus analysis on the random user data in the presence of CSREs. It will be clearly stated for experiments that did not exclusively use the fifth symbol for each radar pulse. Each simulation extracted M symbols for use over the radar CPI.

In order to extract a particular symbol the precise set of samples must be indexed. In order to find the sample index, the timing to the sample index must be calculated. The LTE normal mode timing has fixed definitions that revolve around the fundamental time step, T_s , as explained in Section 2.2.1. For all bandwidth modes, the

fifth symbol sample index (excluding the CP) can be located as follows:

$$Time_{start} = [160 + 4(144 + 2048)]T_s \quad (3.1)$$

$$Sample_{start} = (Time_{start})f_s + 1 \quad (3.2)$$

$$Sample_{end} = Sample_{start} + N_u \quad (3.3)$$

where f_s is the LTE mode sample rate and N_u is the LTE mode number of useful samples. It is important to correctly track symbol sample indices since they vary depending on bandwidth mode. In order to clarify the structure of each pulse in this research, Figure 3.6 depicts the time and frequency domain of the fifth symbol of a 10 MHz mode LTE. Since signal energy is normalized, y-axis values are null.

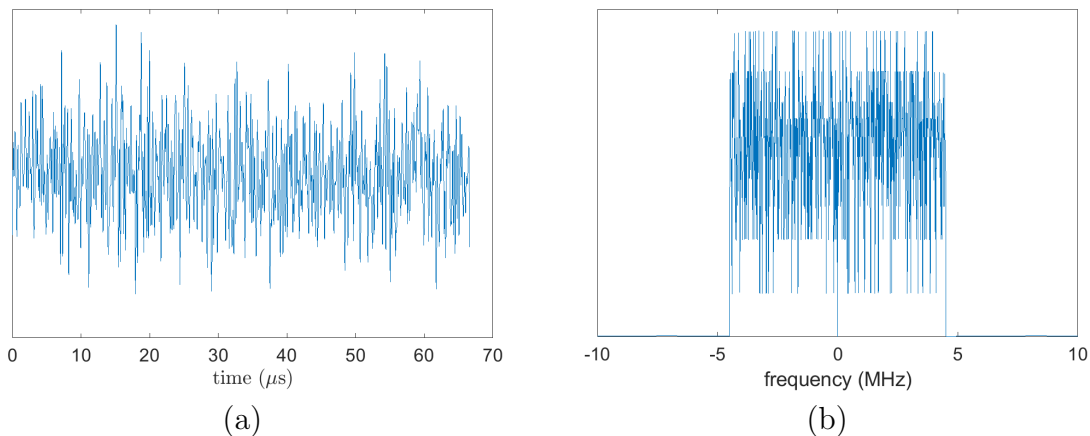


Figure 3.6. (a) Time domain of a radar pulse that is a 10MHz LTE, fifth symbol. (b) Frequency domain magnitude of a radar pulse that is a 10MHz LTE, fifth symbol. Since signal energy is normalized, y-axis values are null.

3.3.2 Radar Bandwidth and Sample Rate Interpolation.

The LTE base station transmit tower can increase and decrease the bandwidth to accommodate variable demand. In order to investigate the effects of variable bandwidth a set of worst-case-scenario experiments were conducted. The worst case

considered varying the bandwidth mode for each pulse. Thus, for the random bandwidth experiments each pulse is considered to be one symbol of randomly varying bandwidth. Future work could investigate how often LTE bandwidth (BW) modes vary and incorporate into experiments.

LTE waveforms need to be interpolated for fast and slow-time experiments where the bandwidth mode varies. The LTE bandwidth modes each have different sample rates, and the MATLAB tool creates digital waveforms with the minimum number of samples required to preserve the information. In order to preserve the information across all BW modes, the radar sample rate must be simulated at the highest bandwidth; thereby preserving Nyquist criteria for the lowest and the highest sample rates. Refer to Table 2.1 for a list of the most common mode sample rates.

In order to accommodate varying sample rates for each simulated LTE waveform, they were interpolated to the highest sample rate, 30.72MHz. Since we want to up-sample to the 20MHz BW mode sample rate, we can divide the 20MHz mode sample rate by each other mode sample rates to find an interpolation factor for each. The digital LTE signals are complex, therefore to interpolate we decompose into real and imaginary components. Each component is interpolated by the factor separately then recombined. After interpolation the signal power is normalized and ready for radar processing.

3.4 STAP Assumptions

Waveform effects on PBR across fast-time, slow-time, and space are examined. This section explains additional assumptions needed for space-time processing. A clutter model and PBR geometry is required in order to add the spatial dimension. The simulations extracted the fifth symbol to represent each pulse as described in Section 3.3.1. The PRF was fixed at 7500 Hz, there were $M = 16$ pulses and $N = 8$

channels for each STAP simulation, and a 10 GHz carrier frequency is assumed.

3.4.1 Geometry.

The PBR is assumed to have multi-channel receiver traveling parallel to the y -axis. It is assumed that the system is in a side-looking configuration with uniform linear channel spacing along the y -axis, recall Figure 2.12. The coordinates are defined such that the receiver is located at $(0,0,h_R)$. The transmitter location is defined by two angles, and the transmitter height, h_T . The first angle defining the transmitter location is the grazing angle between the bistatic baseline, L , and the plane $y = h_T$. Assuming a flat earth model the grazing angle may also be referred to as the elevation angle and is labeled, θ_T . The second is the angle between the x -axis (since the configuration is broadside-looking) and a vector pointing to the x - y transmitter coordinate, and is referred to as azimuth, ϕ_T .

In order to examine waveform effects on SINR, a particular range-azimuth CUT is selected. The general transmitter, receiver, and range azimuth CUT geometry are depicted in Figure 3.7. For all STAP experiments $\theta_T = 45^\circ$, $\phi_T = 0^\circ$, $h_R = 1000\text{m}$, $h_T = 1000\text{m}$. Any particular range-azimuth CUT could be selected, but Figure 3.7 purposefully depicts the CUT to occur along $\phi_T \neq 0^\circ$ in order to emphasize what is ϕ_T . However, the range-azimuth CUT selected for all STAP experiments was at $\phi_T = 0^\circ$, $x_p = 3100\text{m}$, and $y_p = 0\text{m}$.

3.4.2 Clutter.

Modeling clutter is critical to STAP, because clutter is inherently colored across space and time. In general, clutter was modeled as i.i.d. but correlated over space and time. The clutter (and noise) contribution for each range bin must be determined for the model, and is referred to as the clutter space-time snapshot. The clutter

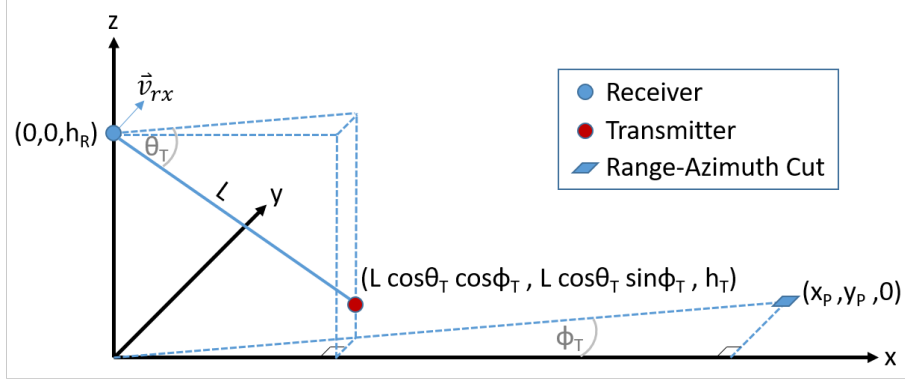


Figure 3.7. Receiver, transmitter, and range/azimuth CUT locations in 3-dimensional coordinates. v_{rx} is along the y-axis, and (x_p, y_p) are the (x, y) coordinates of the range/azimuth CUT location ground patch.

space-time snapshot for the k -th range bin, χ_{ck} , is obtained from

$$\chi_{ck} = \sum_{i=1}^{N_c} \sigma_n^2 \xi_{i,k} \mathbf{v}(\vartheta_{i,k}, \bar{f}_{di,k}), \quad (3.4)$$

where the subscript k denotes the k -th range bin, \mathbf{v} is the space-time steering vector for the i -th k -th clutter patch, N_c is the number of clutter patches being simulated for the range bin, i is the clutter patch index, σ_n^2 is the noise power normalized to 1 Watt for this research, and $\xi_{i,k}$ is the clutter to noise ratio (CNR) for the i -th k -th patch. The CNR provides the clutter contribution to χ_{ck} for each patch and is obtained from,

$$\xi_{i,k} = \frac{P_T G_T(\theta_{T_{i,k}}, \phi_{T_{i,k}}) g_R(\theta_{R_{i,k}}, \phi_{R_{i,k}}) \lambda^2 \sigma_{i,k}}{(4\pi)^3 \sigma_n^2 L_s R_{R_{i,k}}^2 R_{T_{i,k}}^2} \quad (3.5)$$

where P_T is the peak transmit power fixed at 1000 Watts for this research, G_T is the transmitter gain beam pattern and is a function of the transmitter elevation, θ_T , and azimuth, ϕ_T , angles to the i -th k -th clutter patch, g_R is the receiver element gain beam pattern and is a function of the elevation, θ_R , and azimuth, ϕ_R , angles to the i -th k -th clutter patch, σ is the radar cross-section (RCS) of the i - k -th clutter patch, R_R is the range from receiver to the i -th k -th clutter patch, and R_T is the range from

transmitter to i -th k -th clutter patch.

This paragraph provides a brief elaboration on the RCS, σ , from (3.5). The RCS of each patch is independently realized from the same complex normal distribution. The coherency is modeled through the steering vectors that describe the patch's expected coherent change in phase over space and time. The experiments in this research assume zero intrinsic clutter motion and use the in-plane out-of-plane (IPOP) model as carefully described in [4,25]. Briefly, the IPOP models heterogeneous range-dependent clutter based on in-plane out-of-plane scattering properties to assign an expected RCS value to each clutter patch. Details of the model are left to the references. The reason this model was selected was to include the geometrical dependence of clutter and fix the model of choice for all experiments.

Lastly, as described in Section 2.5, transmitter motion induces a structure which manifests as clutter ridge in the angle-Doppler space. The clutter ridge across angle-Doppler space has a slope of 1 ($\alpha = 1$) for this research, with the PRF fixed at 7500 Hz, the carrier wavelength fixed at 0.03 m, and the receiver velocity approximately 112 m/s. The clutter ridge slope is mostly irrelevant since the SINR is analyzed at zero spatial frequency.

Future research needs to verify (3.5) for use with LTE signals. The time-bandwidth product may be a pertinent factor affecting the clutter power contribution from each clutter patch, and (3.5) does not currently account for the waveform time-bandwidth product.

3.4.3 Filter Width.

Available computing power affected the number of samples representing each pulse. In the LTE 20 MHz mode there are 2048 samples per symbol, excluding the CP. This overloaded system memory and required multiple days to perform STAP

and experiment realizations. Thus, the filter width was shortened. For the majority of the STAP experiments, the filter was shortened to approximately $5.4 \mu\text{s}$, which reduced the number of samples in each matched filter response. Additionally, during the execution of STAP experiments, there was a geometry related problem with longer filter lengths. The computing power and geometry problems were eventually overcome to allow full symbol-length pulses and filters. However, unless otherwise stated, the LTE filter lengths were approximately $5.4 \mu\text{s}$.

The next chapter explains each experimental setup and results, building upon the previous chapter theory and the assumptions described in this chapter.

IV. Results & Analysis

4.1 Overview

This chapter explains four particular sets of experiments conducted using LTE waveforms. First, match filtering and Doppler processing is simulated. Second, the effects of randomized bandwidth on match filtering and Doppler processing is explored. After that, bandwidth mode and encoding schemes are varied to examine effects on match filtering. Finally, a three-dimensional geometry is assumed, and a STAP algorithm is applied to the LTE waveforms with varying bandwidth modes (1.4, 3, 5, 10, 15, 20 MHz modes) and encoding schemes (QPSK, 16-ary, and 64-ary). The last section of this chapter describes the computing power required to conduct the experiments.

4.2 Temporal Analysis

A single realization of a M -pulse PBR CPI is simulated using the MATLAB LTE toolbox. Doppler frequencies are normalized, and the PRI is assumed constant. Each pulse contains N_u samples, excluding the CP, of the fifth LTE symbol of each slot. The match filtered sample lag is converted to the bistatic range offset, with zero meters corresponding to zero sample lags. The received waveform is simulated to have no Doppler shift. The slow-time dimension is interpolated to 4096 samples in order to smooth the Doppler processed images. Figures 4.1-4.2 show the resulting match filtered and Doppler processed responses. The figure pixels are arranged similar to the data cube as described in Figure 2.10, and the Doppler processing is executed with a Fourier transform across slow-time of the match filtered response. The y-axes are limited to 1000 meters in order to focus on the region near the main lobes. The most apparent variable feature is the spreading bistatic range offset, which is evident

in the match filtered responses and Doppler processing.

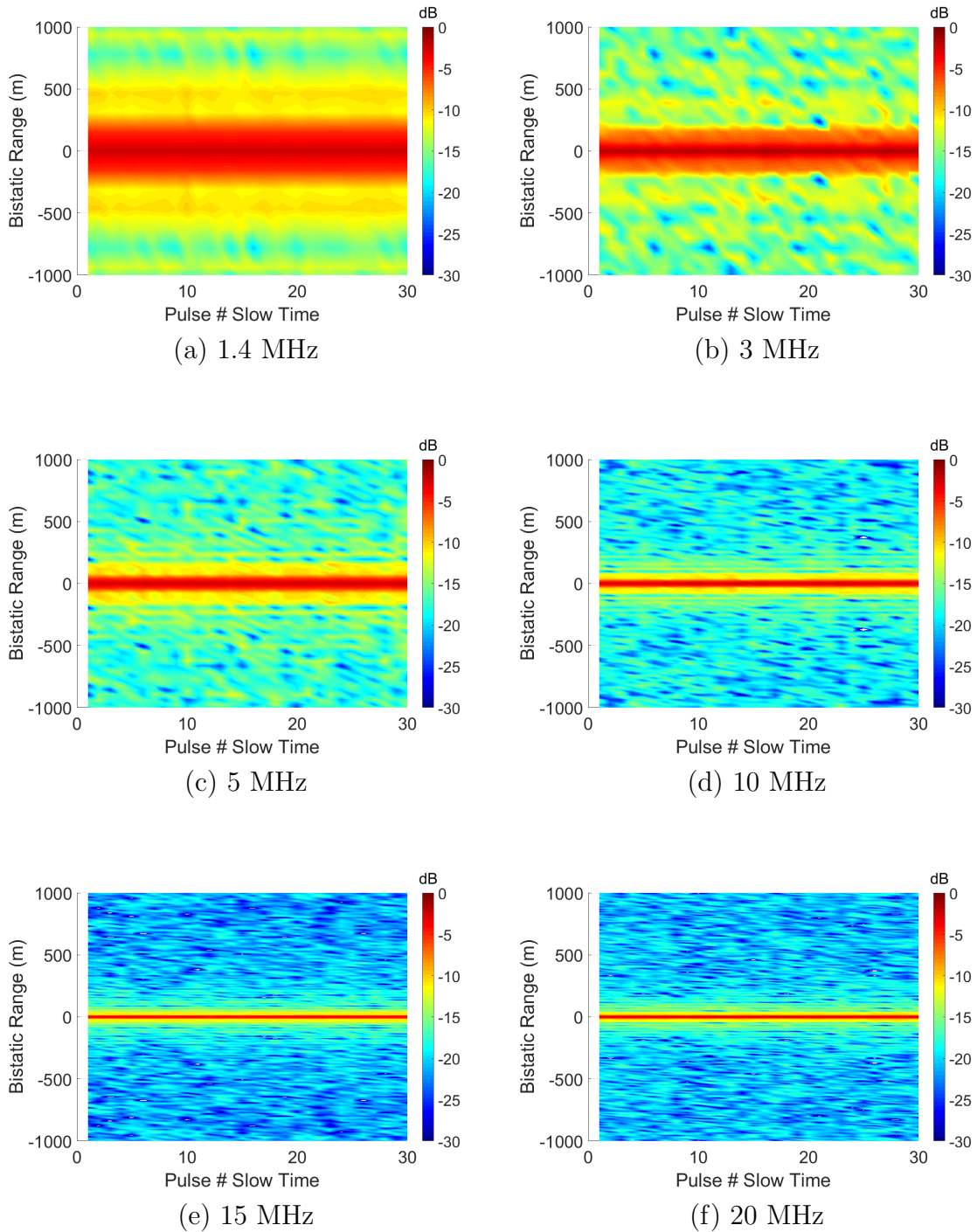


Figure 4.1. Match filtered CPI using each LTE bandwidth mode as the radar pulse signal. The pulse duration is fixed for each bandwidth mode. No noise is included, but pulses vary due to random user data.

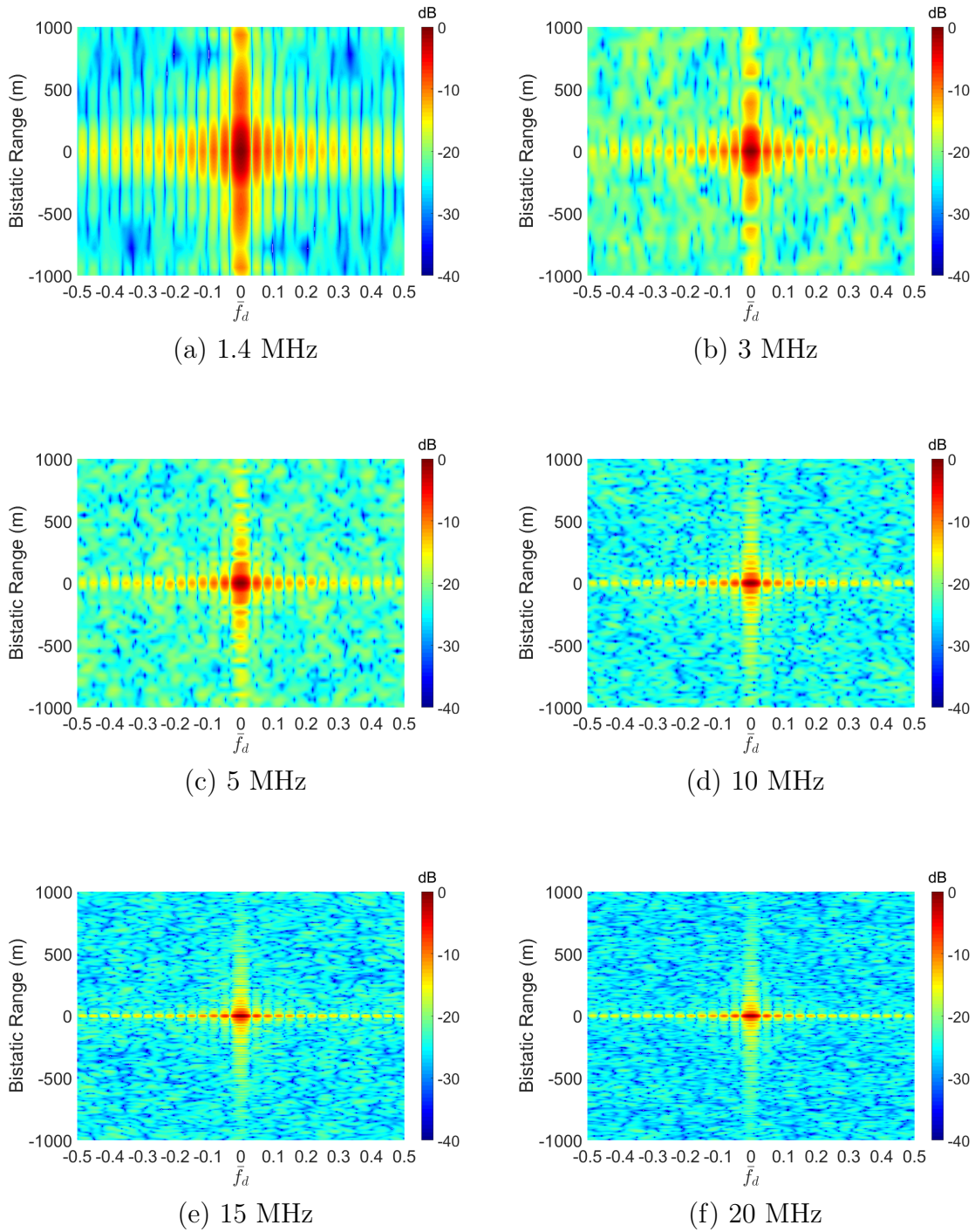


Figure 4.2. Doppler processed CPI using each LTE bandwidth mode as the radar pulse signal. The pulse duration is fixed for each bandwidth mode. No noise is included, but pulses vary due to random user data.

In Figure 4.1 it can be seen that the match filtered main lobe width decreases as the bandwidth mode increases. This is no surprise since it was shown in (2.31) that the range resolution is a function of pulse bandwidth, and a broad main lobe results in higher filter responses adjacent to zero-lag. In Figure 4.2 it can be seen that the Doppler processed responses spread in range, but little or no spreading is evident across Doppler. This is no surprise since the PRI and CPI did not vary, which fixed the Doppler space. These results were critical to understanding basic pulse radar simulations using LTE signals as the pulses, and were foundational to simulations in which the bandwidth varied from pulse to pulse, discussed in the next section.

The following steps summarize the temporal analysis experiment procedure:

1. Set the LTE BW mode.
2. Generate 1 radio frame using LTE toolbox.
3. Use Equations (3.1)-(3.3) to extract and store M fifth symbols.
4. Calculate the fast-time interpolation factor, $\frac{2048}{N_u}$.
5. Split each stored symbol into real and imaginary components. (or use MATLAB *interpft* and skip to normalization step)
6. Interpolate real and imaginary components by interpolation factor.
7. Recombine real and imaginary components.
8. Normalize symbol power, $\mathbf{s} = \frac{\mathbf{s}}{\sqrt{\mathbf{s}^H \mathbf{s}}}$.
9. Perform match filtering across fast-time using MATLAB *xcorr* function, and store results.
10. Set desired slow-time interpolated sample number
11. Perform Doppler processing across slow-time using FFT and slow-time interpolation factor, and store results.

4.3 Random Bandwidth

The results in Section 4.2 Figures 4.1-4.2 suggest that varying LTE bandwidth from pulse-to-pulse may impact expected PBR performance. Thus, the next experiment simulates pulse-varying bandwidth. The bandwidth mode of each pulse varies with uniform randomness between 1.4, 3, 5, 10, and 20 MHz; the 15 MHz mode is excluded to accelerate interpolation processing. All pulses are interpolated to the 20 MHz mode sample rate. Again, as in Section 4.2, the slow-time dimension is interpolated to 4096 samples in order to smooth the Doppler processed images. The y-axes are limited to 2000 meters in order to focus on the region near the main lobes and to capture some sidelobe effects; recall that the full match filtered response is nearly 20,000 meters long. Lastly, for illustrative purposes only, the target is assumed to induce a -0.2 normalized Doppler shift. The Doppler shift is applied by accumulating a -0.2 normalized frequency phase shift per pulse on the received signal, as in (2.8). Figures 4.3 and 4.4 depict 100 pulses match filtered and Doppler processed. Not surprisingly, the match filtered response has substantial main lobe width variation from pulse to pulse. It is a little more difficult to interpret what is happening with the Doppler processing. In both cases, the noise floor has risen in comparison to the fixed mode match filtered and Doppler processed responses. In order to better understand the effects of random bandwidth, a Monte Carlo simulation is necessary.

Next, 400 realizations of match filtered and Doppler processed CPIs are generated. Mean bias and variance convergence were examined for 200 and 300 realizations; bias was minimal and the variance converged, therefore 400 realizations offered reasonable computing power trades. The effects of randomizing the bandwidth from pulse-to-pulse is evident in the match filtered variance and Doppler processing variance (see Figures 4.5 and 4.6).

Since all of the waveforms are normalized, there is minimal variance at 0 lag/bistatic

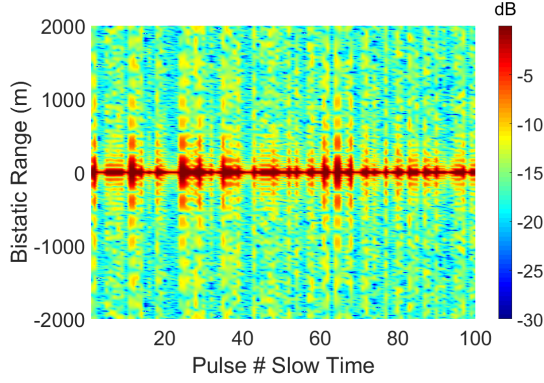


Figure 4.3. 100 match filtered LTE pulses with uniform randomly varying bandwidth.

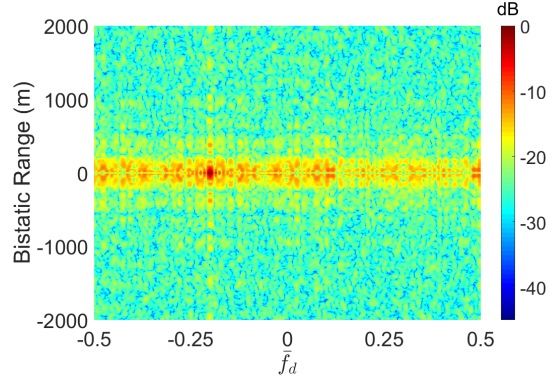


Figure 4.4. 100 Doppler processed LTE pulses with uniform randomly varying bandwidth.

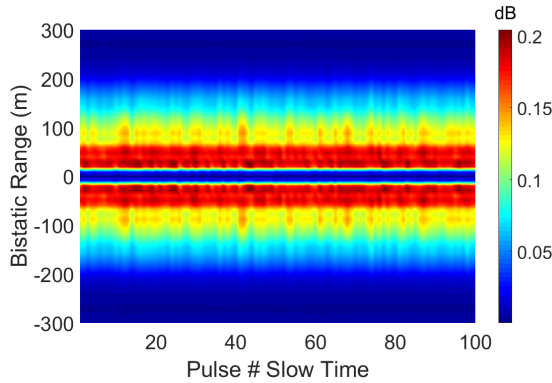


Figure 4.5. Variance of 400 realizations of match filtered LTE pulses with uniform randomly varying bandwidth.

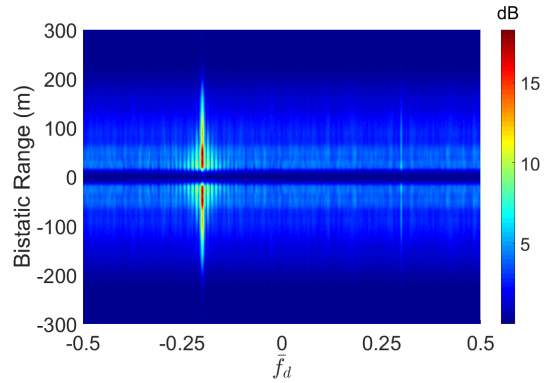


Figure 4.6. Variance of 400 realizations of Doppler processed LTE pulses with uniform randomly varying bandwidth.

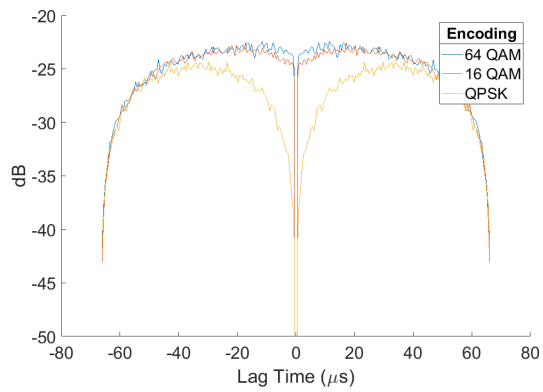
range offset. Once the bistatic range offset is out of the 20 MHz mode mainlobe, match filtered variation rises. From approximately 10 m to 200 m bistatic range offset, the match filtered response variation peaks. Beyond this range, the variation tapers off to zero in the side-lobes. In Figure 4.6 there is a variance spike near $\bar{f}_d = 0.3$ spread along the bistatic range. This variance spike was inexplicable, but multiple Monte Carlo simulations and differing simulated target Dopplers also produced the variance spike.

The following steps summarize the random bandwidth temporal analysis experiment procedure:

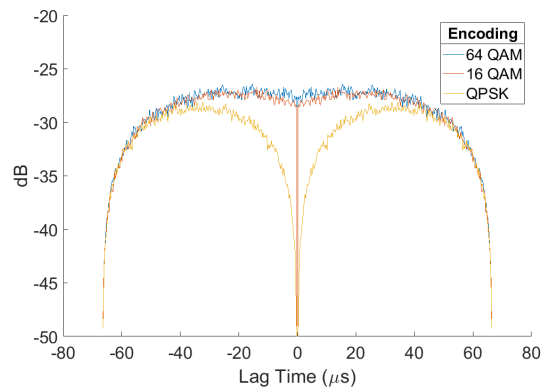
1. Randomly select the LTE BW mode, with uniform random number.
2. Generate 1 radio frame using LTE toolbox.
3. Use Equations (3.1)-(3.3) to extract and store the fifth symbol.
4. Repeat the above steps until M random bandwidth pulses are stored.
5. Calculate the fast-time interpolation factor, $\frac{2048}{N_u}$.
6. Split each stored symbol into real and imaginary components. (or use MATLAB *interpft* and skip to normalization step)
7. Interpolate real and imaginary components by interpolation factor.
8. Recombine real and imaginary components.
9. Normalize symbol power, $\mathbf{s} = \frac{\mathbf{s}}{\sqrt{\mathbf{s}^H \mathbf{s}}}$.
10. Perform match filtering across fast-time using MATLAB *xcorr*, and store results.
11. Set desired slow-time interpolated sample number
12. Perform Doppler processing across slow-time using FFT and slow-time interpolation factor, and store results.
13. Repeat the above steps for 400 realizations and store each realization results.
14. Compute match filter and Doppler processing variance across the 400 realizations.

4.4 Bandwidth and Encoding Scheme Effects on Match Filtering

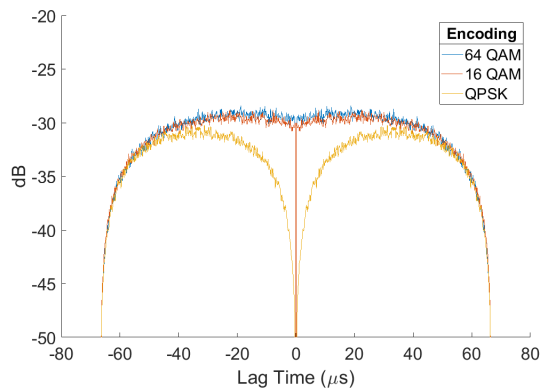
Building upon the results from Sections 4.2 and 4.3, the match filtered sidelobes are more closely examined for each bandwidth mode and user data encoding scheme. For this next analysis, the waveforms are again selected as the fifth symbol, but are not interpolated to remove any unexpected bias that it may introduce. As before, each match filtered response is normalized to the peak response. Figure 4.7 shows the match filtered variances across the three analyzed encoding schemes: QPSK, 16QAM, and 64QAM.



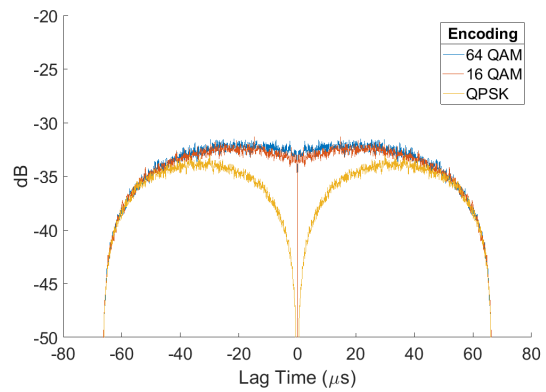
(a) 1.4 MHz



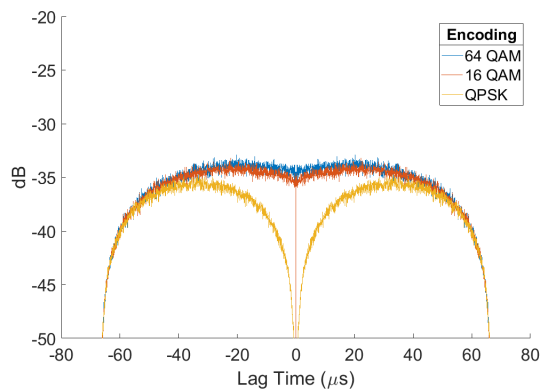
(b) 3 MHz



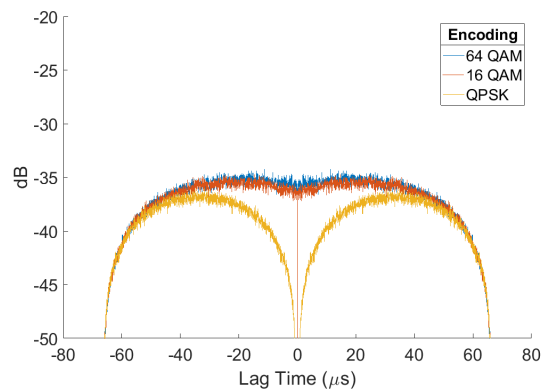
(c) 5 MHz



(d) 10 MHz



(e) 15 MHz



(f) 20 MHz

Figure 4.7. Variance of 200 realizations of match filtered LTEs [1].

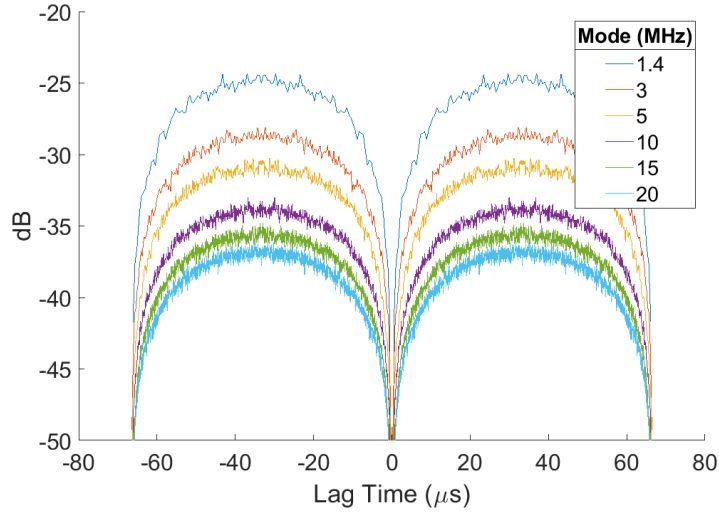


Figure 4.8. Variance of 200 realizations of match filtered QPSK LTEs [1].

The variances were generated from 200 realizations, which was deemed sufficient to minimize mean bias and achieve variance convergence. The match filtered variances are zero at zero lag, due to each waveform being normalized. Inspection of Figure 4.7 show that sidelobe match filtered variance depends on the encoding scheme. The variance increases with encoding scheme; or another way of saying it is that the variance increases with the bit-rate. Examining the variance from zero-lag to around half the maximum lag the differing variance is clear, then tapers off toward the maximum lag. Figure 4.8 it is starkly obvious that match filtered variance is inversely proportional to bandwidth, with the 20 MHz mode having the lowest variance and the 1.4 MHz mode having the highest variance. Since the variance is proportional to the bit-rate and inversely proportional to the bandwidth mode, this suggests there may be an emitter selection/optimization trade-space. The highest bandwidth mode may not always be the best choice signal if there is a lower bandwidth mode available operating at a lower bit-rate.

The following steps summarize the encoding scheme experiment procedure:

1. Select one LTE encoding scheme (QPSK, 16-ary, 64-ary).
2. Select one LTE BW mode (1.4 MHz, 3 MHz, 5 MHz, 10 MHz, 15 MHz, 20 MHz).
3. Generate 1 radio frame using LTE toolbox.
4. Use Equations (3.1)-(3.3) to extract and store the fifth symbols.
5. Perform match filtering across fast-time using MATLAB *xcorr*, normalize with *xcorr*, and store results.
6. Repeat the above steps for 200 realizations and store each realization results.
7. Compute match filter variance across the 200 realizations, and store results.
8. Repeat 2-7 for each BW mode.
9. Repeat 1-7 for each encoding scheme.

4.5 Bandwidth and Encoding Scheme Effects on STAP

Expanding even more upon the prior section results, the SINR performance of the waveform bandwidth modes and encoding schemes are compared. A PBR configuration and geometry is assumed as described in Section 3.4.1, with some key details repeated here: $M = 16$, $N = 8$, the geometry depicted in Figure 3.7, and each pulse is a unique fifth LTE symbol. The filter length was shortened to approximately $5.4 \mu\text{s}$ (rather than using a full $66 \mu\text{s}$ pulse) in order to reduce the processing requirement. The SINR curves were generated from 200 realizations. The mean and standard deviation for the 64QAM 1.4 MHz mode is shown in Figure 4.9; 200 realizations was deemed sufficient to minimize mean bias and achieve variance convergence.

Next, the mean SINR curves for each mode and encoding scheme are shown for convenient comparison in Figures 4.10 and 4.11. Initially, the filter length was shortened to $5\mu\text{s}$ to reduce data processing requirements, but later the filter length was extended to a full LTE pulse length of $66\mu\text{s}$. Extending the filter length allows a

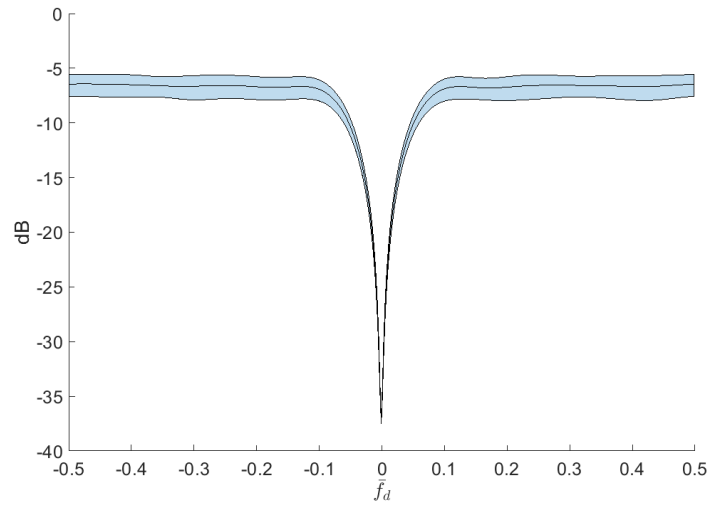


Figure 4.9. Mean and standard deviation of 200 SINR curve realizations. This amount of realizations was sufficient to minimize mean bias and achieve variance convergence.

more accurate representation of the effects of the modeled clutter environment. In Section 4.4 the data suggested the possibility of an emitter selection/optimization trade-space, and Figures 4.10 and 4.11 offer corroboration. There is more SINR loss with higher bit-rates, and more SINR loss with lower bandwidth modes. Therefore the highest bandwidth mode may not always be the best choice signal if there is a lower bandwidth mode available operating at a lower bit-rate. Chapter V will expound upon the significance of these results and describe additional research questions that needing attention.

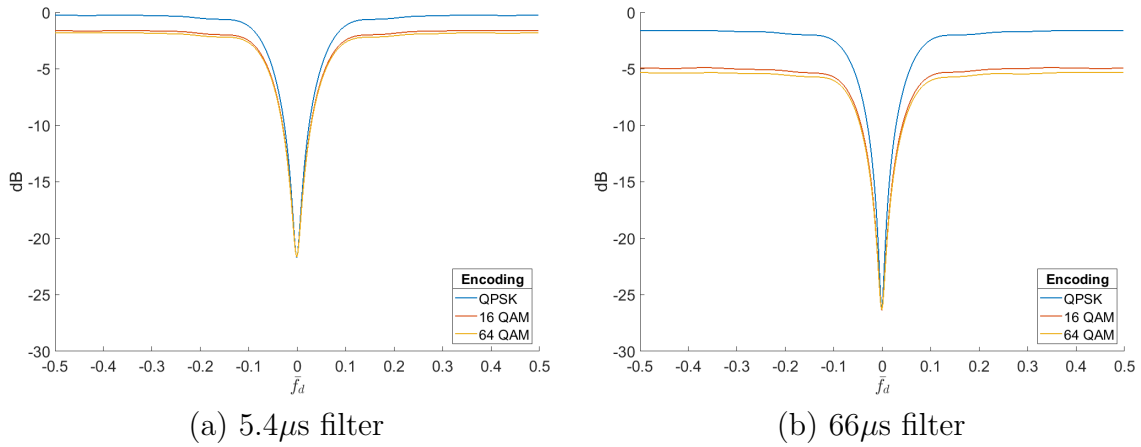


Figure 4.10. Mean SINR_L curves for the LTE 10MHz mode. (a) Has a shorter filter length, which reduced data processing requirements. (b) More accurately represents the effects of the modeled clutter environment.

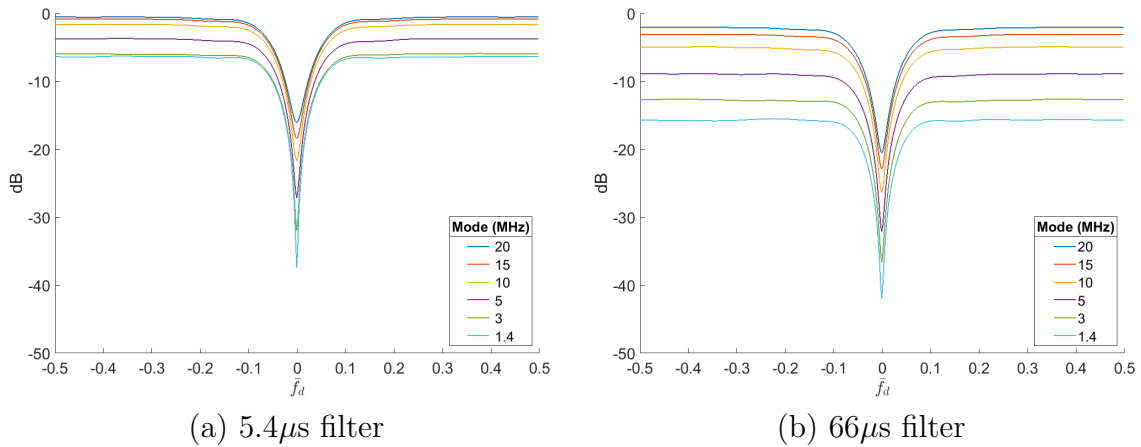


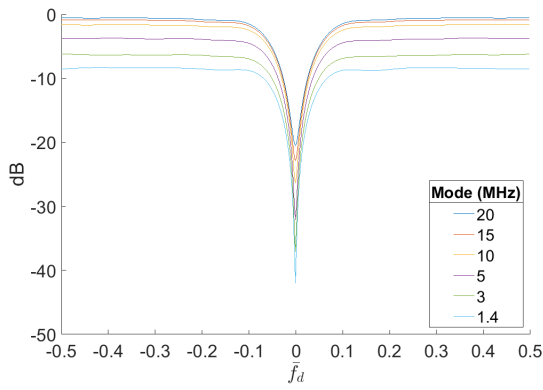
Figure 4.11. Mean SINR_L curves for the 16QAM LTE. (a) Has a shorter filter length, which reduced data processing requirements. (b) More accurately represents the effects of the modeled clutter environment.

The following steps summarize the encoding scheme experiment procedure:

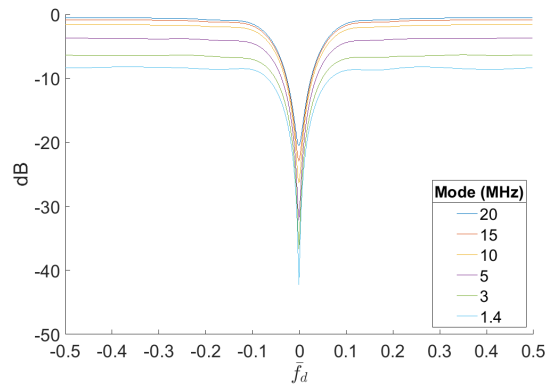
1. Initialize experiment parameters
 - Set BW mode.
 - Set Encoding scheme.
 - Set the number of slow-time pulses, M , and array channels, N .
 - Set clutter to IPOP model.
 - Set range oversampling to 2.
2. Generate 1 radio frame using LTE toolbox.
3. Use Equations (3.1)-(3.3) to extract and store the fifth symbols.
4. Perform match filtering across fast-time using MATLAB *xcorr*, normalize with *xcorr*, and store results.
5. Set match filter extent limit to 800 meter bistatic range offset.
6. Apply the match filter extend limit to prevent memory overload.
7. Craft tapered covariance matrix, \mathbf{R}_k , using equation (2.15).
8. Build space-time steering vector.
9. Calculate the CNR at the range-azimuth CUT using equation (3.5).
10. Calculate the clutter space-time snapshot, $\boldsymbol{\chi}_c$.
11. Calculate SINR loss at the range-azimuth CUT using equation (2.24), and store results.
12. Repeat the above steps for 200 realizations.
13. Compute the standard deviation and average SINR curve, and store results.
14. Repeat the above steps for each mode and encoding scheme combination.

The STAP simulations described prior to this assumed a filter length of approximately $5.4 \mu\text{s}$. The simulation code was improved in order to accommodate longer pulses. The previously described steps were modified by setting the filter extent limit

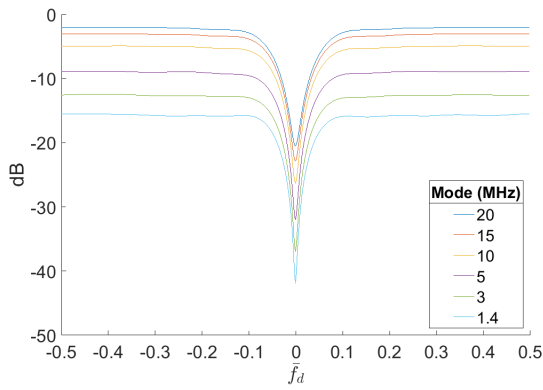
to 9500 m to create full symbol length filter excluding the CP and 10500 m to include the CP. The SINR curves for each mode and encoding scheme for signals with and without the CP are depicted in Figures 4.12-4.13. Comparing left to right, it is evident that the CP has little or no effect on the SINR. All bandwidth modes and encoding schemes are presented for completeness.



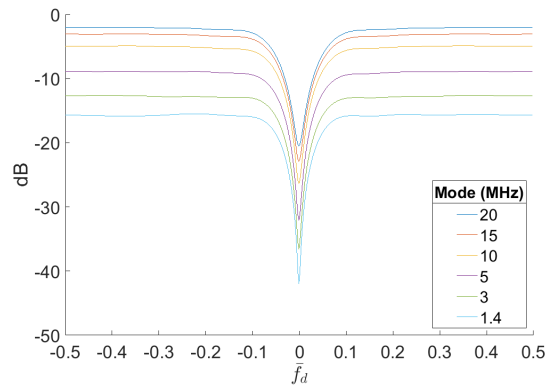
(a) QPSK CP Excluded



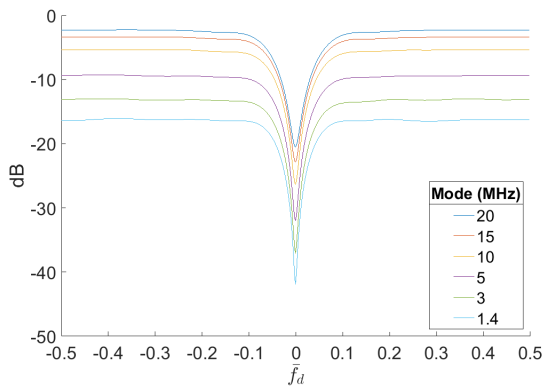
(b) QPSK CP Included



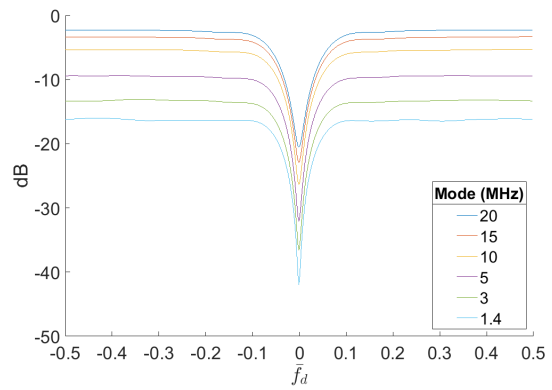
(c) 16QAM CP Excluded



(d) 16QAM CP Included

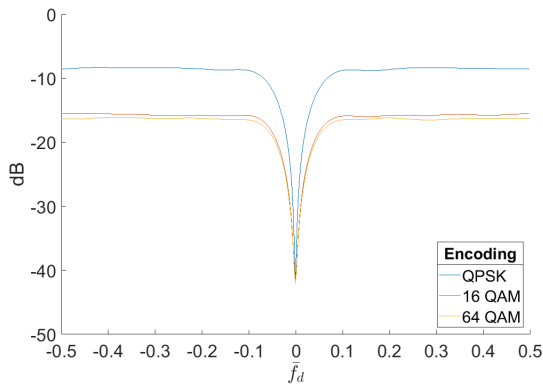


(e) 64QAM CP Excluded

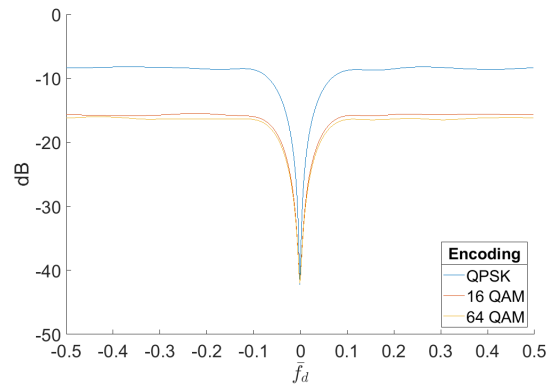


(f) 64QAM CP Included

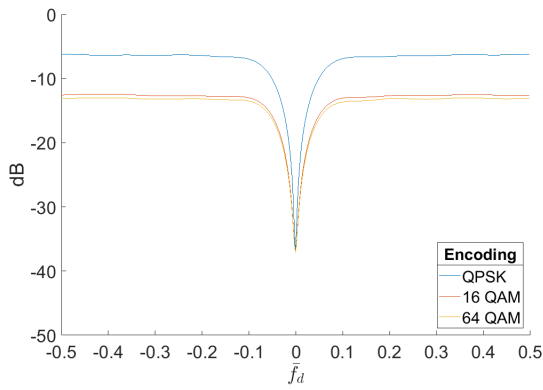
Figure 4.12. Mean SINR_L curves CP excluded (left) and CP included (right) for each LTE mode.



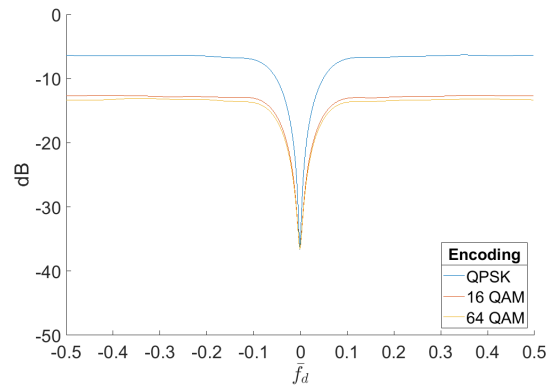
(a) 1.4 MHz Mode CP Excluded



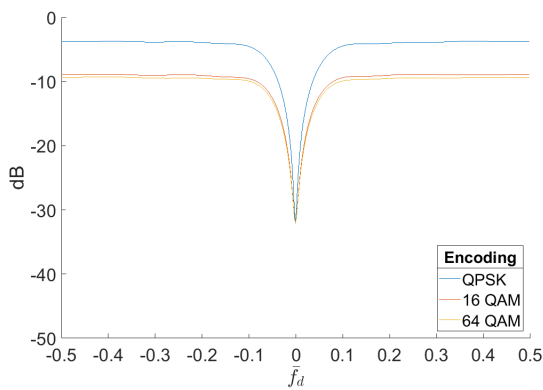
(b) 1.4 MHz Mode CP Included



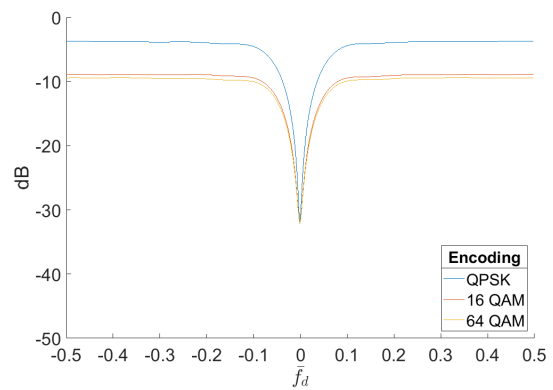
(c) 3 MHz Mode CP Excluded



(d) 3 MHz Mode CP Included

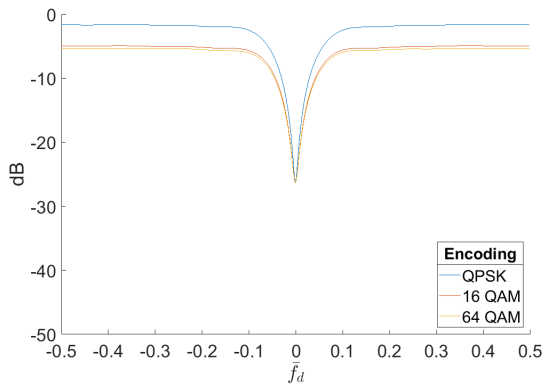


(e) 5 MHz Mode CP Excluded

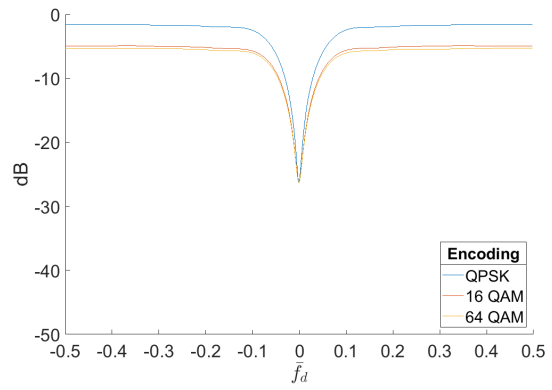


(f) 5 MHz Mode CP Included

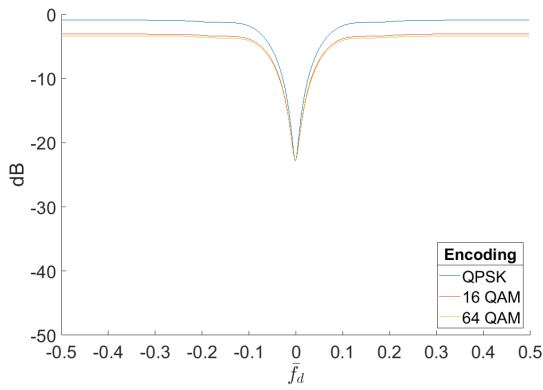
Figure 4.13. Mean SINR_L curves CP excluded (left) and CP included (right) for each encoding scheme; 1.4-5 MHz modes.



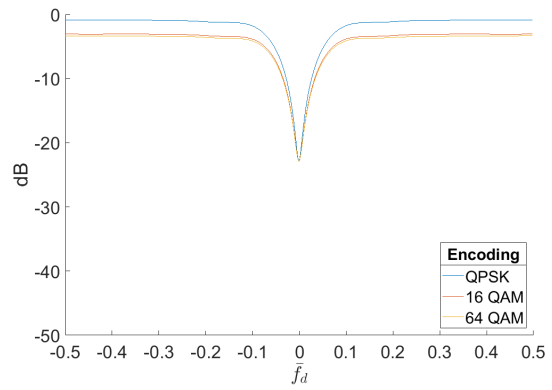
(a) 10 MHz Mode CP Excluded



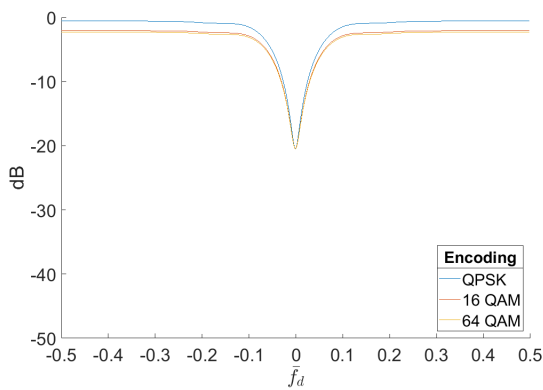
(b) 10 MHz Mode CP Included



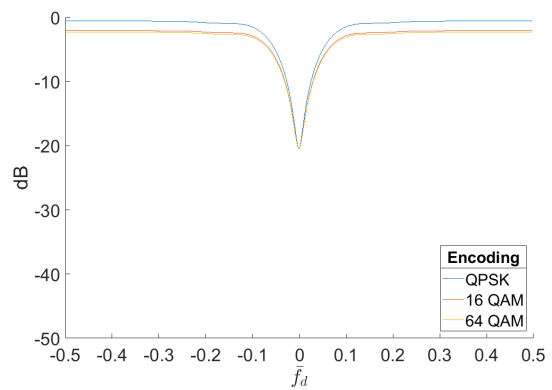
(c) 15 MHz Mode CP Excluded



(d) 15 MHz Mode CP Included



(e) 20 MHz Mode CP Excluded



(f) 20 MHz Mode CP Included

Figure 4.14. Mean SINR_L curves CP excluded (left) and CP included (right) for each encoding scheme; 10-20 MHz modes.

4.6 Computational Resources

The random bandwidth and STAP experiments were constrained by available computing resources. The random bandwidth match filtering and Doppler processing experiments can be completed in one-two hours using a single processing core and requires at least 32 GB of RAM. This is easily available on many AFIT computers; thus, the focus of this section is on the resources required to generate the SINR curves.

The STAP code utilized by this research exploits MATLAB implicit expansion to simulate the radar data-cube, trading high memory costs for faster computation time. Using implicit expansion to simulate the entire range CUT (all normalized Doppler and Azimuth combinations) easily required 196 GB of RAM. Thus, the code was modified in consideration of the required computing power. The number of filter samples was truncated to accommodate the largest number of samples possible without memory overload. The number of samples allowed for the pulse was decided by selecting a maximum bistatic range offset, which was approximately 800 meters, above which the RAM requirement exceeded 196 GB. Additionally, in order to further reduce required computing power, only the 0° range-azimuth CUT was computed.

The STAP code also had a geometry limiting bug, which limited the signal pulse time-length. The bug was encountered when the pulse width exceeded approximately $6 \mu\text{s}$, and resulted in problems modeling \mathbf{R}_k for the particular geometry selected for the simulations (see Section 3.4.1). This limitation was eventually overcome, and results for pulses exceeding $6 \mu\text{s}$ are presented at the end of Section 4.5.

The computation time required to simulate one realization of an entire range CUT was approximately 200 seconds for the 20 MHz mode. Computation time is dependent on the bandwidth mode since the number of samples for each maximum bistatic range offset varies. With a single realization time of 200 seconds for the 20 MHz mode, it required approximately 12 hours to simulate 200 realizations of the 20 MHz mode,

10 hours for 200 realizations of the 15 MHz mode, 8 hours for 200 realizations of the 10 MHz mode, etc. (and note that this is just for one encoding scheme). Bottom line, it easily required a 4 GHz CPU with 196 GB of RAM approximately 5 days to simulate each bandwidth mode and encoding scheme combination.

After limiting the calculations to the 0° range-azimuth CUT, the memory requirement was alleviated. What before took the full 196GB of RAM in the 20 MHz mode, now required approximately 15 GB of RAM, but the computation time did not improve very much. Thus, the simulation was adjusted to run batches of realizations in parallel. This effectively improved the computation time to 20 seconds from 200 seconds for a single 20 MHz mode realization. After these improvements it required approximately 1 hour to simulate 200 realizations of the 20 MHz mode, 0.8 hours for 200 realizations of the 15 MHz mode, etc. Bottom line, it required a 4 GHz CPU with 12 workers and 196 GB of RAM approximately 1 day to simulate each bandwidth mode and encoding scheme combination.

V. Conclusion

5.1 Overview

This chapter revisits the research goal, provides a summary of the results, and contribution to the PBR community. Lastly, future research topics are suggested

5.2 Research Goal

This is a new research area at AFIT, and thus the goals were exploratory. The research focused on LTE waveform affects on PBR, and explored in detail the effects of variable bandwidth, user data encoding, and bandwidth mode on match filtering, Doppler processing and STAP.

5.3 Results and Contribution

A significant portion of work for this research was dedicated to simulating realistic and accurate LTE waveforms. Prior AFIT students, [2], developed an LTE generation tool, but there were tool limitations and uncertainty in the accuracy. Thus, the MATLAB LTE Toolbox was acquired and [8] helped the development of a realistic and accurate waveform. Thus, a side-benefit of this research was improving AFIT LTE simulation capability. Sections 2.2.1 and 3.2 provide detailed break-down of the LTE and a comparison of two generation tools, which will prove beneficial for PBR and communication-centric research.

The research experiment in Section 4.2 was not novel, but an important exploratory step in the overall research. The basic temporal analysis confirmed clutter Doppler spread from pulse diversity due to random user data, as described in [4]. The temporal research also served as a precursor to the random bandwidth experiments. In the beginning phases of this research it was believed that LTE bandwidth could

vary from symbol to symbol. It was later understood that the bandwidth is more likely to vary between radio frames. Thus, the random bandwidth experiments may be less operationally representative, but still provide valuable insights to the worst case scenario. It can be seen in Figures 4.5 and 4.6 that random bandwidth will degrade correct range matching and Doppler estimation.

The STAP experiments examining encoding scheme and bandwidth mode demonstrate the impact of each parameter on SINR loss. This discovery aids PBR flight path optimization, since the best achievable SINR from available signals may be from a waveform at a lower bit-rate. Furthermore, no research at AFIT has yet simulated STAP using LTE waveforms besides [4]. Thus, this research provides an initial stepping stone. The match filtering was limited to center-most samples to accommodate computing limitation, and thus conclusions are limited by this as well.

5.4 Future Research

The following items are a number of areas open to future exploration.

1. Control region effects: The slot preamble and CSREs within the LTE resource grid could be used as the PBR signal.
2. Bandwidth stitching: Base stations may transmit on adjacent carrier frequencies which could be combined to increase effective PBR bandwidth.
3. CP effects: The processing performance losses due to the CP could be characterized. Furthermore, it may be possible to use the CP to improve ranging.
4. Multi-symbol length pulses: Processing multi-symbol length pulses can enable the study of parameter variation (such as bandwidth and encoding) within a PRI.
5. Optimization: the set of signal parameters and geometries could be examined to find what factors matter most for optimization.

6. AFIT tool updates: the AFIT tool could be updated to allow for normal mode LTE signals.
7. PBR in the lab using LTE signals: more consideration must be given the operation of a base station and PBR receiver to address the transmission and collection of a realistic CPI.
8. Varying pulse parameters within one CPI: The effects of varying pulses (such as encoding and bandwidth) within a CPI need to be characterized.
9. Verify (3.5) for use with LTE signals. The time-bandwidth product may be a pertinent factor effecting the clutter power contribution from each clutter patch.

Bibliography

1. F. D. Taylor and J. R. Lievsay, "LTE Bandwidth and Modulation Scheme Effects on Passive Bistatic Radar," in *Asilomar Conference on Signals, Systems, and Computers*, no. 1466, Nov 2018, pp. 1–4.
2. A. Evers and J. A. Jackson, "Analysis of an lte waveform for radar applications," in *2014 IEEE Radar Conference*, May 2014, pp. 0200–0205.
3. ———, "Experimental passive sar imaging exploiting lte, dvb, and dab signals," in *2014 IEEE Radar Conference*, May 2014, pp. 0680–0685.
4. J. R. Lievsay, *Passive Radar Clutter Modeling and Emitter Selection for Ground Moving Target Indication*. University of Oklahoma, PhD Dissertation, 2017.
5. S. Bartoletti, A. Conti, and M. Z. Win, "Passive radar via lte signals of opportunity," in *2014 IEEE International Conference on Communications Workshops (ICC)*, June 2014, pp. 181–185.
6. C. Klöck, V. Winkler, and M. Edrich, "Lte-signal processing for passive radar air traffic surveillance," in *2017 18th International Radar Symposium (IRS)*, June 2017, pp. 1–9.
7. H. D. Griffiths and C. J. Baker, "Passive coherent location radar systems. part 1: performance prediction," *IEE Proceedings - Radar, Sonar and Navigation*, vol. 152, no. 3, pp. 153–159, June 2005.
8. E. Dahlman, S. Parkvall, and J. Skold, *4G, LTE-advanced Pro and the Road to 5G*. Academic Press, 2016.
9. S. D. Blunt and E. L. Mokole, "Overview of radar waveform diversity," *IEEE Aerospace and Electronic Systems Magazine*, vol. 31, no. 11, pp. 2–40, 2016.
10. T. Higgins, S. D. Blunt, and A. K. Shackelford, "Time-range adaptive processing for pulse agile radar," in *2010 International Waveform Diversity and Design Conference*, Aug 2010, pp. 115–120.
11. R. S. A. R. Abdullah, A. A. Salah, A. Ismail, F. Hashim, N. H. A. Aziz, and N. E. A. Rashid, "Ground moving target detection using lte-based passive radar," in *2015 International Conference on Radar, Antenna, Microwave, Electronics and Telecommunications (ICRAMET)*, Oct 2015, pp. 70–75.
12. M. A. Richards, *Fundamentals of radar signal processing*. Tata McGraw-Hill Education, 2005.
13. M. A. Richards, J. A. Scheer, and W. A. Holm, *Principles of Modern Radar, Volume I - Basic Principles*, 2010, vol. I.
14. J. R. Guerci, *Space-time adaptive processing for radar*. Artech House, 2014.
15. W. Melvin and J. Scheer, *Principles of modern radar: advanced techniques*. The Institution of Engineering and Technology, 2012.
16. EUTR, "User equipment (UE) radio transmission and reception (3GPP TS 36.101 version 8.4. 0 release 8)," *ETSI TS*, vol. 136, no. 101, p. V8.

17. Telesystem Innovations, “Telesystem Innovations LTE in a Nutshell,” 2010. [Online]. Available: <https://home.zhaw.ch/kunr/NTM1/literatur/LTE%20in%20a%20Nutshell%20-%20Physical%20Layer.pdf>
18. N. Levanon and E. Mozeson, *Radar signals*. John Wiley & Sons, 2004.
19. J. R. Lievsay, *Simultaneous range/velocity detection with an ultra-wideband random noise radar through fully digital cross-correlation in the time domain*. AFIT, MS Thesis, 2011.
20. I. S. Reed, J. D. Mallett, and L. E. Brennan, “Rapid convergence rate in adaptive arrays,” *IEEE Transactions on Aerospace and Electronic Systems*, no. vol. 6, pp. 853–863, 1974.
21. T. Higgins, K. Gerlach, A. K. Shackelford, and S. D. Blunt, “Aspects of non-identical multiple pulse compression,” in *IEEE National Radar Conference*, 2011.
22. W. L. Melvin, “A STAP overview,” *IEEE Aerospace and Electronic Systems Magazine*, vol. 19, no. 1, pp. 19–35, 2004.
23. J. Ward, “Space-Time Adaptive Processing for Airborne Radar,” 1994.
24. D. V. Nezhin, V. Kostylev, A. Blyakhman, A. Ryndyk, and A. Myakinkov, *Bistatic radar: principles and practice*. Wiley Online Library, 2007.
25. J. R. Lievsay and N. A. Goodman, “Multi-transmitter clutter modeling for passive stap,” in *2016 IEEE Radar Conference*, May 2016, pp. 1–6.

REPORT DOCUMENTATION PAGE

Form Approved
OMB No. 0704-0188

The public reporting burden for this collection of information is estimated to average 1 hour per response, including the time for reviewing instructions, searching existing data sources, gathering and maintaining the data needed, and completing and reviewing the collection of information. Send comments regarding this burden estimate or any other aspect of this collection of information, including suggestions for reducing this burden to Department of Defense, Washington Headquarters Services, Directorate for Information Operations and Reports (0704-0188), 1215 Jefferson Davis Highway, Suite 1204, Arlington, VA 22202-4302. Respondents should be aware that notwithstanding any other provision of law, no person shall be subject to any penalty for failing to comply with a collection of information if it does not display a currently valid OMB control number. **PLEASE DO NOT RETURN YOUR FORM TO THE ABOVE ADDRESS.**

1. REPORT DATE (DD-MM-YYYY) 03-21-2019		2. REPORT TYPE Master's Thesis		3. DATES COVERED (From — To) Sept 2017 — Mar 2019		
4. TITLE AND SUBTITLE Orthogonal Frequency Division Multiplexed Waveform Effects on Passive Bistatic Radar				5a. CONTRACT NUMBER		
				5b. GRANT NUMBER		
				5c. PROGRAM ELEMENT NUMBER		
				5d. PROJECT NUMBER		
				5e. TASK NUMBER		
6. AUTHOR(S) Taylor, Forrest D, Maj				5f. WORK UNIT NUMBER		
				8. PERFORMING ORGANIZATION REPORT NUMBER AFIT-ENG-MS-19-M-058		
						10. SPONSOR/MONITOR'S ACRONYM(S) Intentionally Left Blank
7. PERFORMING ORGANIZATION NAME(S) AND ADDRESS(ES) Air Force Institute of Technology Graduate School of Engineering and Management (AFIT/EN) 2950 Hobson Way Wright-Patterson AFB OH 45433-7765				11. SPONSOR/MONITOR'S REPORT NUMBER(S)		
						9. SPONSORING / MONITORING AGENCY NAME(S) AND ADDRESS(ES) Intentionally Left Blank
12. DISTRIBUTION / AVAILABILITY STATEMENT DISTRIBUTION STATEMENT A: APPROVED FOR PUBLIC RELEASE; DISTRIBUTION UNLIMITED.						
13. SUPPLEMENTARY NOTES						
14. ABSTRACT Communication waveforms act as signals of opportunity for passive radars. However, these signals of opportunity suffer from range-Doppler processing losses due to their high range sidelobes and pulse-diverse waveform aspects. Signals such as the long term evolution (LTE) encode information within the phase and amplitude of the waveform. This research explores aspects of the LTE, such as the encoding scheme and bandwidth modes on passive bistatic Doppler radar. Signal space-time adaptive processing (STAP) performance is evaluated and parameters are compared with the signal to interference-plus-noise ratio (SINR) metric.						
15. SUBJECT TERMS Passive Bistatic Radar						
16. SECURITY CLASSIFICATION OF:			17. LIMITATION OF ABSTRACT UU	18. NUMBER OF PAGES 79	19a. NAME OF RESPONSIBLE PERSON Maj James R. Lievsay, AFIT/ENG	
a. REPORT U	b. ABSTRACT U	c. THIS PAGE U			19b. TELEPHONE NUMBER (include area code) (937) 255-3636, x3369; james.lievsay@afit.edu	